

Thomas Nagel, Norbert Böttcher, Uwe-Jens  
Görke, Olaf Kolditz

**Computational Geotechnics**  
**Storage of Energy Carriers**

31. January 2017

**Springer**

## About the Authors

**Thomas Nagel** is heading the groups “Computational Energy Systems”<sup>1</sup> at the Helmholtz Centre for Environmental Research—UFZ, as well as “Environmental Geotechnics: Multi-physics simulation for geotechnical system analysis”<sup>2</sup>, a joint work group between the UFZ and the Federal Institute for Geosciences and Natural Resources (BGR). He holds an Adjunct Professorship at Trinity College Dublin, Ireland. During his master’s studies of Mechanical Engineering/Applied Mechanics at Chemnitz University of Technology he worked on coupled problems in biomechanics and biomedical technology at Rush University Medical Center in Chicago and Eindhoven University of Technology, the Netherlands. In 2012 he was awarded his PhD from Trinity College Dublin for a dissertation in mechanobiology. Since then he has been working at the UFZ as part of a team of scientists developing the numerical simulation framework OpenGeoSys for coupled multiphysical problems. His particular foci are thermochemical and sensible heat storage in porous media as well as geotechnical applications in the context of energy supply, storage and waste management.

**Norbert Böttcher** is currently working as a scientist at the Federal Institute for Geosciences and Natural Resources (BGR) in Hanover, Germany, and guest scientist at the UFZ. Prior to this, he was a member of the scientific staff of the UFZ Department of Environmental Informatics. After his graduation in Water Supply Management and Engineering, Dr. Böttcher worked at the Institute for Groundwater Management at Dresden University of Technology, Germany, as a lecturer and a research scientist. He received his PhD for developing a mathematical model for the simulation of non-isothermal, compressible multiphase flow processes within the context of subsurface CO<sub>2</sub> storage. His research interests cover coupled THM modelling and model development.

---

<sup>1</sup> <http://www.ufz.de/comp-energy-sys>

<sup>2</sup> <http://www.ufz.de/environmental-geotechnics>

**Uwe-Jens Görke** has been a staff member of the Department of Environmental Informatics since 2008. He studied Theoretical Mechanics and Applied Mathematics at the University of Kharkov, and holds a PhD in Solid Mechanics. From 1996 to 2008 he worked at Chemnitz University of Technology. His research interests are related to numerical methods and constitutive modelling with applications in geo-technologies, particularly focused on energy-related topics, like geothermal energy, energy storage and carbon dioxide storage. Dr. Görke coordinates work packages of different national research projects and is involved in managing projects during all project stages—from the application for funds to final reporting.

**Olaf Kolditz** is the head of the Department of Environmental Informatics at the Helmholtz Center for Environmental Research (UFZ). He holds a Chair in Applied Environmental System Analysis at the Technische Universität in Dresden. His research interests are related to environmental fluid mechanics, numerical methods and software engineering with applications in geotechnics, hydrology and energy storage. Prof. Kolditz is the lead scientist of the OpenGeoSys project<sup>3</sup>, an open-source scientific software platform for the numerical simulation of thermo-hydro-mechanical-chemical processes in porous media, in use worldwide. He studied theoretical mechanics and applied mathematics at the University of Kharkov, got a PhD in natural sciences from the Academy of Science of the GDR (in 1990) and earned his habilitation in engineering sciences from Hannover University (in 1996), where he became group leader at the Institute of Fluid Mechanics. Until 2001 he was full professor for Geohydrology and Hydroinformatics at Tübingen University and director of the international Master course in Applied Environmental Geosciences. Since 2007 he is the speaker of the Helmholtz graduate school for environmental research HIGRADE. Prof. Kolditz is Editor-in-Chief of two international journals *Geothermal Energy* (open access) and *Environmental Earth Sciences* (ISI). Prof. Kolditz is a leading scientist in numerous Sino-German research networks.

---

<sup>3</sup> [www.opengeosys.org](http://www.opengeosys.org)

# Preface

The increasing intensity of the subsurface usage for energy storage, energy “production”, energy waste deposition, resource extraction, infrastructure and many others as part of the ongoing technical development of a growing world population requires a careful assessment of potential environmental consequences to maintain our base of living. The strategies and scenarios required for a sustainable development can be devised and tested with the help of numerical simulations using models of the underlying coupled physical, chemical and biological processes.

Here, subsurface storage of energy carriers is selected as an example technology in this context. In particular, this book presents an introduction to thermo-mechanical modelling of gas storage in salt caverns using the open-source software *OpenGeoSys* (*OGS*). The material is mainly based on work done in the framework of the ANGUS+<sup>4</sup> and NUMTHECHSTORE<sup>5</sup> projects, and is also the result of a close cooperation within the *OGS* community ([www.opengeosys.org](http://www.opengeosys.org)). These voluntary contributions are highly acknowledged.

In the context of subsurface usage in transforming energy systems, the book features a general introduction to gas storage in rock salt formations, the constitutive modelling of rock salt, and the coupling of heat transport with solid mechanical problems. It contains several step-by-step guides on how to set up models of both laboratory experiments and real-scale caverns with OGS.

This book is intended primarily for graduate students and applied scientists dealing with coupled problems in the subsurface, in particular those interested in applying a freely available and customizable open-source simulation framework in their research. As such, this book will be a valuable help in the training of geomechanical modelling and provides an entry point to a modelling tool which is expandable and highly flexible.

---

<sup>4</sup> <http://angusplus.de/en>

<sup>5</sup> <http://www.ufz.de/index.php?en=37528>

This tutorial is the fourth volume in the Springer series *Computational Modeling of Energy Systems*<sup>6</sup> that presents applications of computational modelling in energy sciences. Within this series, this volume opens up a sequel of contributions on applying the simulation platform OGS to geotechnical applications in the energy sector based on work performed in close cooperation with the Federal Institute for Geosciences and Natural Resources (BGR)<sup>7</sup>:

- ▷ Computational Geotechnics: Storage of Energy Carriers, this volume,
- ▷ Computational Geotechnics: Deep Geological Repositories, Nagel et al. (2018\*).

It was preceded by three tutorials in the series covering the topic geothermal energy

- ▷ Geoenergy Modeling I. Geothermal Processes in Fractured Porous Media<sup>8</sup> (Böttcher et al., 2016),
- ▷ Geoenergy Modeling II. Shallow Geothermal Systems<sup>9</sup> (Shao et al., 2016),
- ▷ Geoenergy Modeling III. Enhanced Geothermal Systems<sup>10</sup> (Watanabe et al., 2017).

and will also feature technical applications, such as

- ▷ Models of Thermochemical Heat Storage, Lehmann et al. (2017\*).

These contributions are related to a similar publication series in the field of environmental sciences, namely:

- ▷ Computational Hydrology I: Groundwater Flow Modeling<sup>11</sup> (Sachse et al., 2015),
- ▷ Computational Hydrology II<sup>12</sup> (Sachse et al., 2017),
- ▷ OGS Data Explorer, Rink et al. (2017\*),

(\*approximate publication time).

Few books are without errors, and this book is likely no exception. Should you discover errors that should be corrected, we would be grateful if you let us know and help improve this book.

---

<sup>6</sup> <http://www.springer.com/series/15395>

<sup>7</sup> <http://www.ufz.de/environmental-geotechnics>

<sup>8</sup> <http://www.springer.com/de/book/9783319313337>

<sup>9</sup> <http://www.springer.com/de/book/9783319450551>

<sup>10</sup> <http://www.springer.com/de/book/9783319465791>

<sup>11</sup> <http://www.springer.com/de/book/9783319133348>

<sup>12</sup> <http://www.springer.com/de/book/9783319528083>

Preface

ix

Leipzig, January 2017

*Thomas Nagel*  
*Uwe-Jens Görke*  
*Olaf Kolditz*  
*Norbert Böttcher*

Hannover, January 2017



# Acknowledgements

We deeply acknowledge the *OpenGeoSys* community for their continuous support to the *OpenGeoSys* development activities and thank Francesco Parisio for valuable comments on Chapter 3. The authors would gratefully like to acknowledge the funding provided by the German Ministry of Education and Research (BMBF) for the ANGUS+ project, grant number 03EK3022, as well as the support of the Project Management Jülich (PtJ). Additional funding was provided by the Helmholtz Initiating and Networking Fund through the NUMTHECHSTORE project.





# Contents

<b>1</b>	<b>Introduction</b> .....	1
1.1	Energetic use of the subsurface .....	1
1.2	Geotechnical use of rock salt .....	2
1.3	Gas storage in salt caverns .....	3
1.4	Scope and structure of this tutorial .....	5
<b>2</b>	<b>Basics of thermo-mechanics and inelasticity</b> .....	7
2.1	Governing equations .....	7
2.2	Finite element implementation and the Kelvin mapping .....	10
2.3	Integration of inelastic constitutive models .....	13
2.4	Thermo-mechanical coupling in OGS .....	16
2.5	Constitutive models .....	17
<b>3</b>	<b>Simulation of laboratory tests</b> .....	23
3.1	Non-isothermal triaxial creep test .....	23
3.2	Triaxial test with plasticity .....	36
<b>4</b>	<b>Simulating Gas Storage in Salt Caverns</b> .....	47
4.1	Scenario .....	47
4.2	General set-up .....	49
4.3	Isothermal model set-up .....	57
4.4	Non-isothermal model set-up .....	59
4.5	Comparison of results .....	61
<b>5</b>	<b>Closing remarks</b> .....	67
	<b>References</b> .....	69



# Chapter 1

## Introduction

### 1.1 Energetic use of the subsurface

The rising energy demand of the growing world population is a significant cause for environmental risks associated with harmful emissions, hazardous waste, destructive land use, etc. This creates a pressing need to avoid or resolve conflicts between a continuing socio-technical development on the one hand and the preservation of the natural basis of our existence on the other. In order to build an ecologically, economically and socially sustainable future, environmental, climate and energy policies are targeting measures such as the decarbonisation of the energy system, resource efficiency and sustainability, while maintaining energy security. Achieving these goals entails the growing use of renewable energy sources and highly efficient energy conversion technologies. Current concepts of future energy systems and infrastructures link natural and technical systems in an interactive manner. There is a strong need for methods and tools to design and assess technological options for future energy systems as well as their environmental impact. This holds particularly true for technologies involving the geo-environment.

The increasing intensity of the subsurface usage for energy storage, energy “production”, energy waste deposition, resource extraction, infrastructure and many others requires novel science-based strategies for regulatory bodies, businesses and stakeholders alike (Bauer et al., 2013; Kabuth et al., 2016). Such strategies and scenarios can be developed and tested with the help of numerical simulations using models of the underlying coupled physical, chemical and biological processes.

Underground storage of energy carriers encompasses numerous geological repositories such as rock caverns, salt caverns, porous formations, aquifers, etc., as well as different forms of energy and energy carriers, namely thermal energy, potential energy (compressed air) and chemical energy (hydrogen, natural gas, oil).

In this contribution, the focus is on gas storage in rock salt caverns in the context of energy transitions to renewable sources. Fig. 1.1 gives an impression of a cavern field in a rock salt dome.

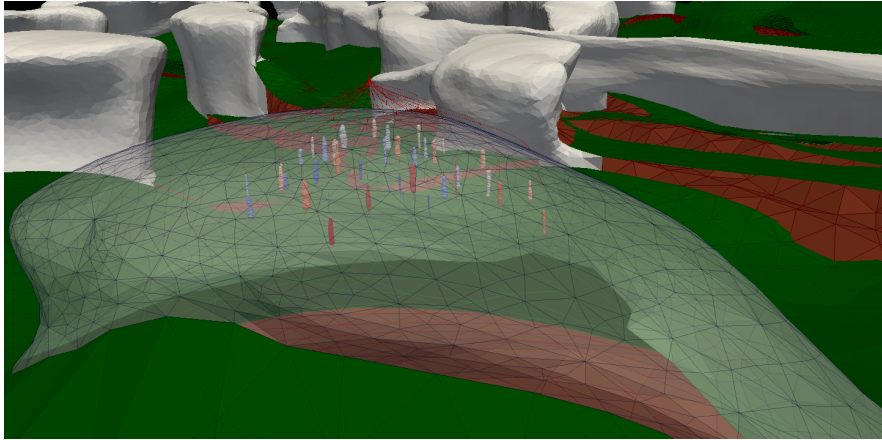


Fig. 1.1: Impression of a cavern field in a salt dome/diapir.

## 1.2 Geotechnical use of rock salt<sup>13</sup>

Interest in the mechanical behaviour of rock salt formations can on the one hand be attributed to the mining of salt, and is on the other hand associated with the formations' increasing use for geotechnical applications (Minkley et al., 2015b). The tight morphology of rock salt makes it an ideal material for the storage of matter (Minkley et al., 2013, 2015a). Solution-mined caverns in underground salt domes (Fig. 1.1) have been used for the storage of strategic oil and gas reserves for decades. Salt rock is also under discussion as a candidate repository formation for hosting nuclear and other types of waste (Harris et al., 2015; Hunsche and Schulze, 1994; Li et al., 2015; Pudewills et al., 1995; Xing et al., 2015). In the context of the transition to volatile renewable energies, compressed air energy storage (CAES) in salt caverns is discussed to mitigate fluctuations in wind energy for a continuous and reliable electricity production (Greenblatt et al., 2007; Ibrahim et al., 2008; Lund and Salgi, 2009; Lund et al., 2009; Ma et al., 2015; Safaei et al., 2013). Finally, the cavern storage of hydrogen as a chemical energy carrier produced electrolytically from renewable energy sources has gained scientific

<sup>13</sup> For an extended version of this section, see Nagel et al. (2017).

interest (Böttcher et al., 2017; Crotogino et al., 2010; Minkley et al., 2013; Ozarslan, 2012).

The safety of salt mines as well as the long-term convergence behaviour of salt caverns has been assessed based on thermo-mechanical models capturing the inelastic behaviour of rock salt (Cristescu, 1985; Hunsche and Schulze, 1994; Lux, 1984; Lux and Rokahr, 1984; Ma et al., 2015; Pudewills, 2005; Pudewills and Droste, 2003). Rock salt is a material exhibiting several modes of creep and plasticity (Cristescu, 1994; Cristescu and Hunsche, 1998). Different, usually viscoplastic, salt models have been developed in the past in order to represent the mechanical characteristics of rock salt under laboratory and field conditions (Chan et al., 1994; Desai and Zhang, 1987; Hampel et al., 2010; Heusermann et al., 1983; Jin and Cristescu, 1998; Minkley, 2004; Minkley et al., 2001; Minkley and Mühlbauer, 2007). Lately, in the context of the novel applications outlined above, an increased and broader interest into the mechanical behaviour of rock salt due to a more intense use of the subsurface for energy storage and conversion has developed. These novel applications also shift the focus of the analyses somewhat from the long-term behaviour to short-term phenomena induced on the time scale relevant for renewable energy applications (Li et al., 2015; Minkley et al., 2015a). For example, while the time scales of pressure changes in caverns used for strategic oil and gas reserves or seasonal energy storage concepts are on the order of months and years, caverns of CAES power plants have to withstand significant pressure fluctuations several times a day or week (Böttcher et al., 2017; Greenblatt et al., 2007).

Convergence can drastically reduce cavern volume (Wang et al., 2011). Fluid percolation (Minkley et al., 2015a) and cracks induced by thermo-mechanical loading (Sicsic and Bérest, 2014) are other aspects relevant from both economic and safety perspectives necessitating stability analyses (Heusermann et al., 2003; Lux, 1984; Ma et al., 2015). Material models are a decisive factor for the reliability of any geotechnical safety assessment (Kolymbas et al., 2016).

### 1.3 Gas storage in salt caverns

Bridging gaps in supply and demand ensuring continuity and predictability of energy supply, providing black-start capabilities, coupling of different energy sectors and increasing energy efficiency are among the pertinent reasons to employ energy storage technologies. Energy storage furthermore avoids over-dimensioning by making it possible to operate transmission and distribution grids with lighter designs (Ibrahim et al., 2008). Operated for so-called load levelling, it helps to reduce fluctuations, thereby making the supply more predictable as well as assisting in power quality control (Ibrahim et al., 2008). Depending on the operation mode, working gas, and intended

system service, caverns can serve short-, medium- and long-term storage purposes (Böttcher et al., 2017; Greenblatt et al., 2007). Cavern storage is—like pumped hydropower—one of the few utility-scale storage options providing capacities in the TWh range.

Potential energy can be stored in the form of compressed air in caverns. The idea for CAES stems from the use of 60-70 % of the available power for the compression of the combustion air in a standard gas turbine. “It therefore seems possible, by separating the processes in time, to use electrical power during off-peak hours (storage hours) in order to compress the air, and then to produce, during peak hours (retrieval hours), three times the power for the same fuel consumption by expanding the air in a combustion chamber before feeding it into the turbines” (Ibrahim et al., 2008).

CAES can facilitate the integration and higher penetration of renewable sources into current energy systems (Greenblatt et al., 2007; Safaei et al., 2013). Its efficiency is largely determined by waste heat recovery and scalable heat storage technologies (Safaei et al., 2013), and its economic feasibility strongly depends on the design of the electricity market (Lund and Salgi, 2009).

Several CAES plants are under operation (Huntorf in Germany, McIntosh in Alabama, USA) while others are in a planning or construction stage (Greenblatt et al., 2007). Huntorf became operational as the first CAES plant in 1978, consists of two salt caverns with a combined 310,000 m<sup>3</sup> operated at 44-70 bar, and can provide up to 290 MW at full capacity for four hours at a discharge flow rate of 417 kg/s (Safaei et al., 2013). McIntosh, operational since 1991, has one salt cavern of 540,000 m<sup>3</sup> with pressures of 45-74 bar providing 110 MW at full capacity for 26 hours at an air discharge rate of 154 kg/s (Safaei et al., 2013).

Another way of storing energy in salt caverns is by using chemical energy carriers. Power-to-gas usually refers to the production of hydrogen (and possibly the subsequent conversion to methane) from electricity. It is increasingly discussed and tested internationally in the context of the transition to sustainable energy systems and in conjunction with fuel cells or even a hydrogen-based economy (Adamson, 2004; Gahleitner, 2013). Fig. 1.2 illustrates a number of usage chains for the hydrogen produced from renewable energy.

In a system where hydrogen is produced in large quantities from renewable energies, large-scale storage options are required. It seems plausible to transfer the experience from natural gas storage to the storage of hydrogen in salt caverns for different periods of time (Crotagino et al., 2010; Ozarslan, 2012). Competing storage technologies are available and a thorough comparison—considering technical, economical and environmental aspects—is required (Taylor et al., 1986). The results of current European projects indicate that while many aspects require further R&D, cavern storage of hydrogen is technically feasible, the geological prerequisites are met in many

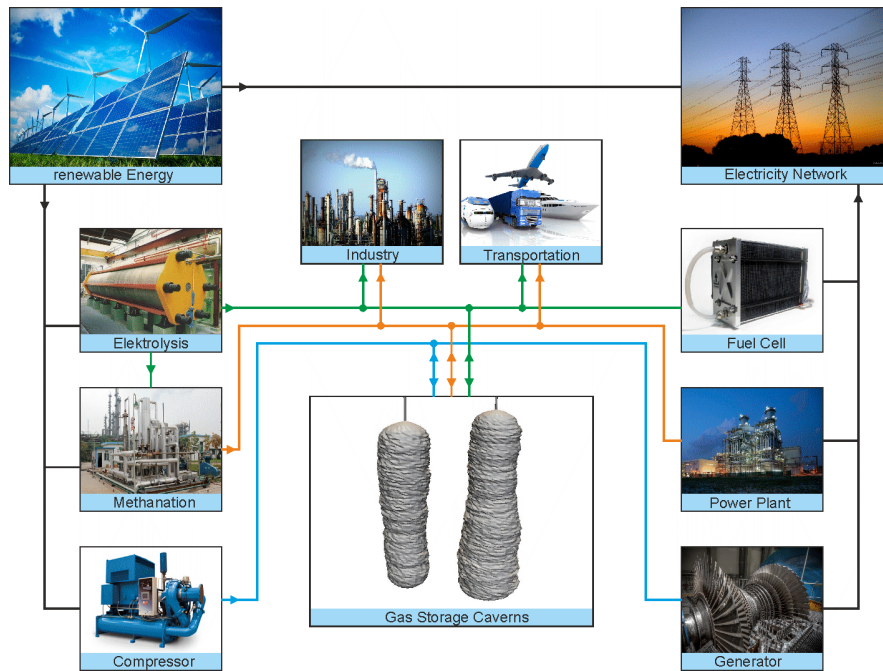


Fig. 1.2: Illustration of power-to-gas(-to-power) conversion chains.

countries, and it adds comparatively little cost to the overall hydrogen-centred value chain; cf. <http://hyunder.eu/>.

## 1.4 Scope and structure of this tutorial

This tutorial-style book gives a concise introduction into the following aspects of modelling and simulation of geotechnical gas storage in rock salt caverns:

- ▷ The basics of coupling thermal and mechanical problems in a continuum setting along with the finite element implementation of the resulting initial boundary value problems, particularly in OpenGeoSys, are reviewed in Chapter 2. This includes aspects of the Kelvin mapping.
- ▷ Chapter 2 also describes inelastic material models for capturing viscoelastic and viscoplastic features of rock salt deformation behaviour and their fully implicit numerical integration in OpenGeoSys.
- ▷ The simulation of rock laboratory-type element tests (isothermal and non-isothermal triaxial tests) used for the basic assessment of material behaviour as well as for parameter identification in existing constitutive models is described in Chapter 3.

- ▷ Finally, a near real-world complexity example of setting up a fully coupled thermo-mechanical analysis of hydrogen storage in a salt cavern is provided in Chapter 4. Based on an initially defined scenario, isothermal and non-isothermal analyses are compared with respect to their predictions.

In this context, “tutorial-style” implies that the necessary basic theoretical background is provided without dwelling on too much details to be found elsewhere, and that the simulation examples are presented with the intention of being reproducible for somebody who has not worked with OpenGeoSys before. For this purpose, input files are explained where necessary as well as provided online<sup>14</sup>, and a step-by-step approach with try-it-yourself features is taken in various examples of differing complexity. All simulations are down-sized from more complex analyses so that they can be run on standard computers in a short time and require no special features without sacrificing their practical relevance.

Where appropriate, references are made to the new version of OpenGeoSys, OGS-6, which is currently becoming available for the kind of analyses described in this book.

---

<sup>14</sup> <https://docs.opengeosys.org/books>

## Chapter 2

# Basics of thermo-mechanics and inelasticity

Rock salt can undergo large inelastic deformations over extended periods of time. Many analyses, however, refer to time intervals and mechanical loads that cause deformations for which the small-strain assumption remains valid. Here, we restrict ourselves to such small-strain settings and postpone analyses under finite deformations to a follow-up contribution (compare also Fig. 2.1).

OGS mainly offers the analysis types 3D, 2D plane strain and axisymmetric. In the sequel, a general tensorial notation is chosen for the field equations while finite element concepts are presented in a three-dimensional setting only. For special considerations in the context of lower-dimensional or analyses relying on special symmetries, we refer the reader to standard textbooks (Bathe, 2014; Zienkiewicz et al., 2005-2006), the benchmark book series (Kolditz et al., 2012, 2016, 2014) or the source code documentation of OGS<sup>15</sup>.

OGS offers the possibility to couple mechanical analyses to thermal, hydraulic and chemical processes using either sequential or monolithic schemes. Here, the focus is on thermo-mechanical couplings.

### 2.1 Governing equations

In a finite-strain setting, the material is mapped to different geometrical configurations as it deforms and evolves over time. The two most relevant configurations are the current and the reference configuration, cf. Fig. 2.1. The different configurations lead to a multitude of stress and strain measures. In a small-strain setting, we assume that the reference configuration (often taken as the undeformed state for convenience) changes only very slightly. Thus, particles are assigned only their reference coordinates, now designated by  $\mathbf{x}$ , and field gradients are evaluated exclusively with respect to those coordinates.

---

<sup>15</sup> <https://doxygen.opengeosys.org/>

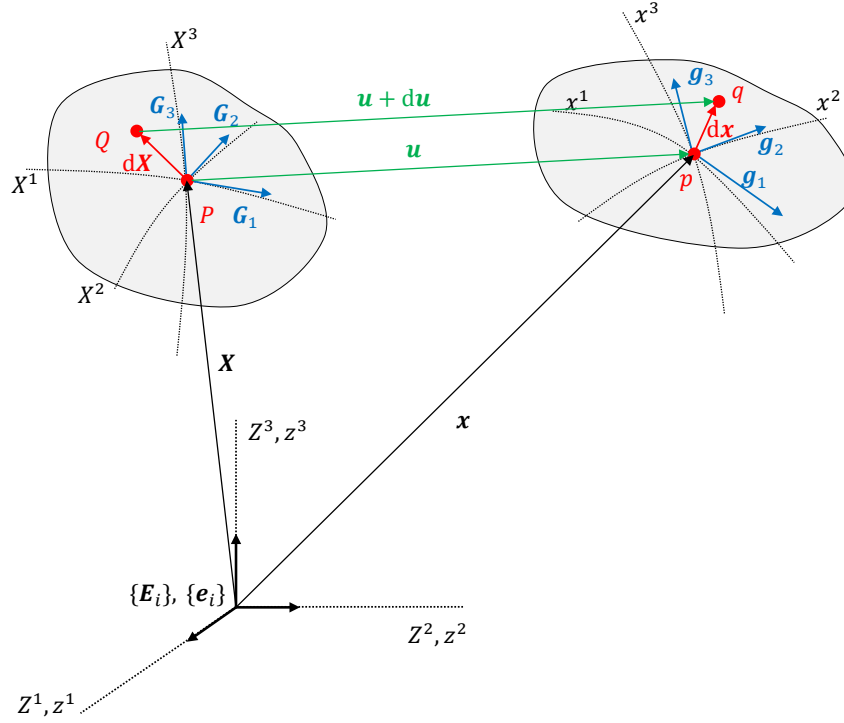


Fig. 2.1: Material points move from their reference placement  $\mathbf{X}$  to their current placement  $\mathbf{x}$ , both of which are connected by the displacement vector  $\mathbf{u}$ . Neighbouring material points define material line elements represented by  $d\mathbf{X}$  and  $d\mathbf{x}$  in the reference and current configurations, respectively. Curvilinear  $(X^I, x^i)$  and Cartesian  $(Z^I, z^i)$  coordinate lines define local basis systems for the geometrical description of the motion problem. For further details, see Haupt (2002); Holzapfel (2000); Hutter and Jöhnk (2004).

The relevant strain measure is the small-strain tensor  $\boldsymbol{\epsilon} = \text{sym grad } \mathbf{u}$ , the relevant stress measure the Cauchy stress tensor  $\boldsymbol{\sigma}$ . The initial boundary value problem is thus defined on a (reference) domain  $\Omega$  as indicated in Fig. 2.2.

To perform a basic thermo-mechanical analysis in a quasistatic small-strain setting we employ the local (PDE) forms of the equilibrium conditions (derived from the balance of momentum) and the heat conduction equation (derived from the balance of energy)

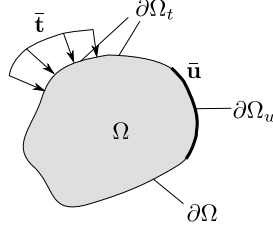


Fig. 2.2: Domain  $\Omega$  with prescribed displacements  $\bar{\mathbf{u}}$  on the Dirichlet boundary  $\partial\Omega_u$  and prescribed tractions  $\bar{\mathbf{t}}$  on the Neumann boundary  $\partial\Omega_t$ . Similar boundaries can be defined for the thermal problem, where a given temperature  $\bar{T}$  is prescribed on the Dirichlet boundary  $\partial\Omega_T$  and a normal heat flux  $\bar{q}_n$  is prescribed on the Neumann boundary  $\partial\Omega_q$ .

$$\mathbf{0} = \operatorname{div} \boldsymbol{\sigma} + \rho \mathbf{b} \quad (2.1)$$

$$0 = \rho c_p \frac{\partial T}{\partial t} + \operatorname{div} \mathbf{q} \quad (2.2)$$

together with the boundary and initial conditions

$$\mathbf{u} = \bar{\mathbf{u}} \quad \forall \mathbf{x} \in \partial\Omega_u \quad (2.3)$$

$$\boldsymbol{\sigma} \cdot \mathbf{n} = \bar{\mathbf{t}} \quad \forall \mathbf{x} \in \partial\Omega_t \quad (2.4)$$

$$T = \bar{T} \quad \forall \mathbf{x} \in \partial\Omega_T \quad (2.5)$$

$$-\mathbf{q} \cdot \mathbf{n} = \bar{q}_n \quad \forall \mathbf{x} \in \partial\Omega_q \quad (2.6)$$

$$\mathbf{u}(t=0) = \mathbf{u}_0 \quad \forall \mathbf{x} \in \Omega \quad (2.7)$$

$$T(t=0) = T_0 \quad \forall \mathbf{x} \in \Omega \quad (2.8)$$

where the boundary domains fulfill the conditions

$$\partial\Omega = \partial\Omega_u \cup \partial\Omega_t = \partial\Omega_T \cup \partial\Omega_q$$

$$\emptyset = \partial\Omega_u \cap \partial\Omega_t = \partial\Omega_T \cap \partial\Omega_q$$

In preparation of a finite element implementation, Eqs. (2.1) and (2.2) are cast into their weak forms. For that purpose we introduce the function *ansatz* and test spaces

$$\mathbf{V}_u^a = \{\mathbf{v} \in \mathbf{H}^1(\Omega) : \mathbf{v} = \bar{\mathbf{u}} \quad \forall \mathbf{x} \in \partial\Omega_u\}$$

$$V_T^a = \{v \in H^1(\Omega) : v = \bar{T} \quad \forall \mathbf{x} \in \partial\Omega_T\}$$

$$\mathbf{V}_u^t = \{\mathbf{v} \in \mathbf{H}^1(\Omega) : \mathbf{v} = \mathbf{0} \quad \forall \mathbf{x} \in \partial\Omega_u\}$$

$$V_T^t = \{v \in H^1(\Omega) : v = 0 \quad \forall \mathbf{x} \in \partial\Omega_T\}$$

With  $\mathbf{u} \in \mathbf{V}_u^a$ ,  $T \in V_T^a$ ,  $\mathbf{v}_u \in \mathbf{V}_u^t$  and  $v_T \in V_T^t$  we find the weak forms

$$\int_{\Omega} \boldsymbol{\sigma} : \text{grad } \mathbf{v}_u \, d\Omega = \int_{\partial\Omega_t} \bar{\mathbf{t}} \cdot \mathbf{v}_u \, d\Gamma + \int_{\Omega} \mathbf{b} \cdot \mathbf{v}_u \, d\Omega \quad (2.9)$$

$$\int_{\Omega} \rho c_p \frac{\partial T}{\partial t} v_T \, d\Omega - \int_{\Omega} \mathbf{q} \cdot \text{grad } v_T \, d\Omega = \int_{\partial\Omega_q} q_n v_T \, d\Omega \quad (2.10)$$

As will be outlined in Section 2.4, a uni-directional staggered coupling scheme will be used to solve the coupled problem given by Eqs. 2.9 and 2.2. Non-linear constitutive equations for the stresses (cf. Section 2.3) motivate an incremental-iterative approach. Based on a known solution at time  $t$ , the solution in the next time increment  $t + \Delta t$  will be determined iteratively by a Newton-Raphson scheme. For that purpose, a linearisation of Eq. 2.9 is performed around the current state identified by the (global Newton) iteration counter  $i$ , leading to the linearised weak form

$$\begin{aligned} \int_{\Omega} \text{grad } \mathbf{v}_u : \left. \frac{d\boldsymbol{\sigma}}{d\boldsymbol{\epsilon}} \right|_i : \Delta \boldsymbol{\epsilon}^{i+1} \, d\Omega = \\ \int_{\partial\Omega_t} \bar{\mathbf{t}}^{t+\Delta t} \cdot \mathbf{v}_u \, d\Gamma + \int_{\Omega} \mathbf{b}^{t+\Delta t} \cdot \mathbf{v}_u \, d\Omega - \int_{\Omega} \boldsymbol{\sigma}^i : \text{grad } \mathbf{v}_u \, d\Omega \end{aligned} \quad (2.11)$$

where

$$\boldsymbol{c} = \frac{d\boldsymbol{\sigma}}{d\boldsymbol{\epsilon}} \quad (2.12)$$

is the fourth order constitutive stiffness tensor.

In the present coupling scheme and for the constitutive assumptions made here, no such step is necessary for Eq. 2.10.

## 2.2 Finite element implementation and the Kelvin mapping

### *The Kelvin mapping of tensorial quantities*

Commonly, the transition to a standard matrix–vector notation in the context of finite element implementations is performed by replacing three-dimensional symmetric second-order tensors by six-dimensional vectors (using engineering shear strains  $\gamma_{ij} = 2\epsilon_{ij}$ ) and three-dimensional fourth-order tensors by  $6 \times 6$  matrices. This *Voigt mapping* leads to a different treatment of, e.g., stresses and strains and does not preserve tensor norms. Here, the *Kelvin mapping* will be preferred which introduces a new 6D basis  $\{\mathbf{E}_I\}$  such that the tensor character of all quantities is preserved.

In terms of implementation, OGS-5 is set up using the Voigt mapping with only a few material models integrated with an experimental Kelvin mapping scheme. The integration relies on appropriate transformation routines for both mappings. OGS-6 is entirely designed both in its core and in the implemented constitutive models using the Kelvin mapping.

One possible way of arriving at the Kelvin mapping is to consider the eigenvalue problem of fourth-order tensors in analogy to the more familiar version for second-order tensors. Without going into details, which can be found in Nagel et al. (2016), the super-symmetric fourth-order symmetry projection tensor  $\mathcal{T}^s$  with the property  $\mathcal{T}^s : \mathbf{A} = \text{sym } \mathbf{A}$  can be written in a Cartesian basis  $\{\mathbf{e}_i\}$  and by using  $\mathbf{I} = \mathbf{e}_i \otimes \mathbf{e}_i$  as

$$\mathcal{T}^s = \mathbf{I} \circledast \mathbf{I} = \frac{1}{2} [\mathbf{e}_i \otimes \mathbf{e}_j \otimes \mathbf{e}_i \otimes \mathbf{e}_j + \mathbf{e}_i \otimes \mathbf{e}_j \otimes \mathbf{e}_j \otimes \mathbf{e}_i] \quad (2.13)$$

an has the six eigentensors (Itskov, 2009):

$$\begin{aligned} \mathbf{M}_1 &= \mathbf{e}_1 \otimes \mathbf{e}_1 & \mathbf{M}_4 &= \frac{1}{\sqrt{2}} (\mathbf{e}_1 \otimes \mathbf{e}_2 + \mathbf{e}_2 \otimes \mathbf{e}_1) \\ \mathbf{M}_2 &= \mathbf{e}_2 \otimes \mathbf{e}_2 & \mathbf{M}_5 &= \frac{1}{\sqrt{2}} (\mathbf{e}_2 \otimes \mathbf{e}_3 + \mathbf{e}_3 \otimes \mathbf{e}_2) \\ \mathbf{M}_3 &= \mathbf{e}_3 \otimes \mathbf{e}_3 & \mathbf{M}_6 &= \frac{1}{\sqrt{2}} (\mathbf{e}_1 \otimes \mathbf{e}_3 + \mathbf{e}_3 \otimes \mathbf{e}_1) \end{aligned} \quad (2.14)$$

These eigentensors can be viewed as the basis of the Kelvin mapping. Instead of simply reordering tensor coordinates as done in the Voigt mapping, the Kelvin mapping proceeds from the introduction of a new 6D basis  $\{\mathbf{E}_I\}$  based on the original 3D basis  $\{\mathbf{e}_i\}$  (compare Mehrabadi and Cowin (1990)) by setting

$$\mathbf{E}_I = \mathbf{M}_I(\mathcal{T}^s) \quad \forall I = 1, \dots, 6 \quad (2.15)$$

In other words, this basis is identical to the eigentensors of the symmetry projection tensor  $\mathcal{T}^s$ , compare Eq. (2.14).

Thus, exemplary tensors with the necessary symmetries can equivalently be written in the various bases

$$\mathbf{A} = A_{ij} \mathbf{e}_i \otimes \mathbf{e}_j = A_I \mathbf{E}_I \quad \text{with} \quad A_I = \mathbf{A} : \mathbf{E}_I \quad (2.16)$$

$$\mathcal{A} = A_{ijkl} \mathbf{e}_i \otimes \mathbf{e}_j \otimes \mathbf{e}_k \otimes \mathbf{e}_l = A_{IJ} \mathbf{E}_I \otimes \mathbf{E}_J \quad \text{with} \quad A_{IJ} = \mathbf{E}_I : \mathcal{A} : \mathbf{E}_J \quad (2.17)$$

At this stage, we introduce the following short-hand for the vector of tensor coordinates  $A_I$  of a second-order tensor in the Kelvin basis:  $\underline{A}$ . Similarly, the matrix of tensor coordinates  $A_{IJ}$  of a fourth-order tensor in the Kelvin basis will be abbreviated by  $\mathbb{A}$ .

One can see that, similar to the Voigt mapping, the coordinates of second- and fourth-order tensors can now be represented as six-dimensional vectors and matrices. However, the tensor character of all quantities is still preserved. Note further, that the coordinates of the Kelvin mapping of a fourth-order tensor  $\mathbf{A} \otimes \mathbf{A}$  simply follow from the coordinate matrix of the dyadic product of the Kelvin mapped vectors. Thus, the same notation can be employed in both cases.

For numerical implementation, the coordinates of the Kelvin-mapped stress and strain tensors can now be used in a vector format

$$\sigma_{ij} \rightarrow \underline{\sigma} = \left[ \sigma_{11} \ \sigma_{22} \ \sigma_{33} \ \sqrt{2}\sigma_{12} \ \sqrt{2}\sigma_{23} \ \sqrt{2}\sigma_{13} \right]^T \quad (2.18)$$

$$\epsilon_{ij} \rightarrow \underline{\epsilon} = \left[ \epsilon_{11} \ \epsilon_{22} \ \epsilon_{33} \ \sqrt{2}\epsilon_{12} \ \sqrt{2}\epsilon_{23} \ \sqrt{2}\epsilon_{13} \right]^T \quad (2.19)$$

which have the same structure regardless of whether they are stresses or strains. This has the important consequence that tensor norms are preserved when using the Kelvin mapping. This further simplifies the implementation of constitutive models as it makes any distinction of stress- or strain-type quantities entering mathematical operations obsolete (Nagel et al., 2016).

### *Finite element implementation*

The domain of interest is split into standard finite elements characterised by a set of nodal shape functions  $N^a(\mathbf{x})$ . The sought solution vector  $\underline{u}$  (for a more uniform notation we write  $\underline{u}$  even though no Kelvin mapping is performed on the original vector  $\mathbf{u}$ ) in a point is approximated by

$$\underline{u} \approx \tilde{\underline{u}} = \sum_a^{n_n} N^a \hat{\underline{u}}_a = \mathbb{N} \hat{\underline{u}} \quad (2.20)$$

where

$$\hat{\underline{u}} = [\hat{u}_1^1 \cdots \hat{u}_1^{n_n} \ \hat{u}_2^1 \cdots \hat{u}_2^{n_n} \ \hat{u}_3^1 \cdots \hat{u}_3^{n_n}]^T \quad (2.21)$$

is the nodal displacement vector of the element containing the point at which  $\underline{u}$  is evaluated,  $\mathbb{N}$  is the element matrix of shape functions and  $n_n$  is the number of nodes of said element. In the isoparametric concept employed here, the position vector  $\underline{x}$  and the test function  $v$  are approximated likewise. Similarly, the  $\mathbb{B}$ -matrix containing the gradients of the shape functions can be introduced to enable the calculation of strain vectors from the nodal displacements (for details see, e.g., Zienkiewicz et al. (2005-2006)):

$$\underline{\epsilon} = \text{sym grad } \underline{u} = \mathbb{B} \hat{\underline{u}} \quad \text{and} \quad \text{sym grad } v = \mathbb{B} \hat{v} \quad (2.22)$$

with the slightly modified  $\mathbb{B}$ -matrix

$$\mathbb{B}_0 = \begin{pmatrix} N_{,1}^1 & \dots & N_{,1}^{n_n} & 0 \dots 0 & 0 \dots 0 \\ 0 \dots 0 & N_{,2}^1 & \dots & N_{,2}^{n_n} & 0 \dots 0 \\ 0 \dots 0 & 0 \dots 0 & 0 \dots 0 & N_{,3}^1 & \dots & N_{,3}^{n_n} \\ [N_{,2}^1 & \dots & N_{,2}^{n_n}] / \sqrt{2} & [N_{,1}^1 & \dots & N_{,1}^{n_n}] / \sqrt{2} & 0 \dots 0 \\ 0 \dots 0 & [N_{,3}^1 & \dots & N_{,3}^{n_n}] / \sqrt{2} & [N_{,2}^1 & \dots & N_{,2}^{n_n}] / \sqrt{2} \\ [N_{,3}^1 & \dots & N_{,3}^{n_n}] / \sqrt{2} & 0 \dots 0 & [N_{,1}^1 & \dots & N_{,1}^{n_n}] / \sqrt{2} \end{pmatrix} \quad (2.23)$$

Substitution of these relations into Eq. (2.11) allows the elimination of the arbitrary nodal values  $\hat{u}$  of the test functions and produces the equation system for each elemental domain  $\Omega^e$ :

$$\int_{\Omega^e} \mathbb{B}^T \mathbb{C}^i \mathbb{B} \, d\Omega \, \Delta \hat{u}^{i+1} = \int_{\partial \Omega_\ell^e} \mathbb{N}^T \bar{\ell}^{t+\Delta t} \, d\Gamma + \int_{\Omega^e} \mathbb{N}^T \rho \underline{b}^{t+\Delta t} \, d\Omega - \int_{\Omega^e} \mathbb{B}^T \underline{\sigma}^i \, d\Omega \quad (2.24)$$

The integral on the left-hand side defines the stiffness matrix  $\mathbb{K}$ , the right-hand side defines the residual vector  $\underline{\psi}$  such that the linearised system reads

$$\mathbb{K}^i \Delta \hat{u}^{i+1} = \underline{\psi}^i \quad (2.25)$$

The contributions of all elements are assembled into the global problem which is then solved for the vector of unknown displacement increments  $\Delta \hat{u}^{i+1}$ .

In summary, a constitutive equation for the stresses is required to correctly calculate the residual vector  $\underline{\psi}^i$  on the right-hand side of Eq. (2.24) as well as the usually solution dependent  $\mathbb{C}^i$ -matrix containing the material moduli in an algorithmically consistent manner (Simo and Hughes, 1998).

For similar finite element schemes in a finite-strain setting see, e.g., Bathe (2014); Görke et al. (2010, 2012); Zienkiewicz et al. (2005-2006). For an extension of the Kelvin mapping to the finite-strain context refer to Nagel et al. (2016).

## 2.3 Integration of inelastic constitutive models

### *General aspects*

In order to determine the stresses  $\underline{\sigma}^i$  and the stiffness tensor  $\mathbb{C}^i$  or, more accurately, their coordinate matrices in Kelvin mapping  $\underline{\sigma}^i$  and  $\mathbb{C}^i$  from Eq. (2.24), constitutive relations are required.

In the linear elastic case, stress follows directly—independent of loading path and rate—from strain and the stiffness matrix has constant entries, rendering Eq. (2.24) linear. The tensorial relations for linear elasticity (using the Lamé constants)

$$\boldsymbol{\sigma} = \lambda(\boldsymbol{\epsilon} : \mathbf{I})\mathbf{I} + 2\mu\boldsymbol{\epsilon} \quad (2.26)$$

$$\mathbb{C} = \lambda\mathbf{I} \otimes \mathbf{I} + 2\mu\mathbf{I} \odot \mathbf{I} \quad (2.27)$$

hold independent of the particular tensor basis (i.e., also for the Kelvin mapping) and translate into the following Kelvin-mapped tensor coordinate matrices:

$$\underline{\boldsymbol{\sigma}} = \begin{pmatrix} 2\mu\epsilon_{11} + \lambda\text{tr } \boldsymbol{\epsilon} \\ 2\mu\epsilon_{22} + \lambda\text{tr } \boldsymbol{\epsilon} \\ 2\mu\epsilon_{33} + \lambda\text{tr } \boldsymbol{\epsilon} \\ 2\mu\sqrt{2}\epsilon_{12} \\ 2\mu\sqrt{2}\epsilon_{23} \\ 2\mu\sqrt{2}\epsilon_{13} \end{pmatrix} = \lambda(\underline{\boldsymbol{\epsilon}} \cdot \underline{\mathbf{I}})\underline{\mathbf{I}} + 2\mu\underline{\boldsymbol{\epsilon}} \quad (2.28)$$

$$\underline{\mathbb{C}} = \begin{pmatrix} 2\mu + \lambda & \lambda & \lambda & 0 & 0 & 0 \\ \lambda & 2\mu + \lambda & \lambda & 0 & 0 & 0 \\ \lambda & \lambda & 2\mu + \lambda & 0 & 0 & 0 \\ 0 & 0 & 0 & 2\mu & 0 & 0 \\ 0 & 0 & 0 & 0 & 2\mu & 0 \\ 0 & 0 & 0 & 0 & 0 & 2\mu \end{pmatrix} \quad (2.29)$$

Considering general inelastic material models, these constitutive relationships follow from a set of differential and algebraic equations (DAEs) of varying non-linearity. In other words, stresses don't follow in an explicit manner from total strains and the stiffness matrix is no longer constant.

### *Integration algorithm*

In order to efficiently solve the non-linearities a local Newton-Raphson procedure is introduced consistent with its global equivalent. *Local* in this context refers to performing the stress integration in each integration point of the quadrature rule employed to numerically approximate the integrals in Eq. (2.24) by sums. *Global* refers to the entire equation system (2.25) assembled over all finite elements of the domain. More details on the following can be found in Nagel et al. (2017) and the references therein.

The differential-algebraic equation system necessary for the integration of the stress increments is compactly written as

$$\underline{\mathbf{0}} = \underline{\mathbf{r}}(\underline{\mathbf{z}}, \underline{\boldsymbol{\epsilon}}^i) \quad (2.30)$$

where  $\underline{\mathbf{r}}$  represents the residual vector describing the evolution equations for stresses and internal variables, as well as constraints (e.g., the consistency condition in elasto-plasticity). Note that in the local iterations to solve the

above equation system,  $\underline{\epsilon}^i$  from the global iteration is considered fixed. The state vector  $\underline{z}$  contains the stress vector as well as the constitutive model's internal state variables ( $\underline{\kappa}_k, \kappa_k$ ):

$$\underline{z} = (\underline{\sigma}^T, \underline{\kappa}_k^T, \kappa_k)^T \quad (2.31)$$

The evolution equations most often involve rates in the form of first order time derivatives. Considering the general ordinary differential equation

$$\dot{y} = f(y) , \quad (2.32)$$

time discretisation of the rate quantities in the functionals is based here on a generalised single step scheme. We write for a time step in the interval  $[t, t + \Delta t]$

$$y^{t+\Delta t} = y^t + \Delta t [\alpha f^{t+\Delta t} + (1 - \alpha) f^t] \quad (2.33)$$

which includes the schemes

$$\alpha = \begin{cases} 0 & \text{Euler forward (explicit)} \\ 0.5 & \text{Crank-Nicolson} \\ 1 & \text{Euler backward (implicit)} \end{cases} \quad (2.34)$$

With this relationship, a rate of change at time  $t + \Delta t$  can be approximated based solely on known quantities and the unknown primary variable at time  $t + \Delta t$ :

$$\dot{y}^{t+\Delta t} = \frac{y^{t+\Delta t} - y^t}{\alpha \Delta t} - \frac{y^t}{\alpha \Delta t} - \frac{1 - \alpha}{\alpha} f^t \quad (2.35)$$

Note that for  $\alpha = 0$ , the above relationship cannot be used directly but the rate at time  $t$  is used directly and exclusively. A Taylor series expansion of the differential-algebraic system yields the iteration procedure for the local stress integration

$$-\underline{r}^j = \left. \frac{\partial \underline{r}}{\partial \underline{z}} \right|_j \Delta \underline{z}^{j+1} \quad (2.36)$$

It shall be mentioned here that the resulting solution update can be damped by a factor  $\alpha_{\text{LS}}$  determined from a line-search procedure

$$\underline{z}^{j+1} = \underline{z}^j + \alpha_{\text{LS}} \Delta \underline{z}^{j+1} \quad (2.37)$$

where  $\alpha_{\text{LS}} \in (0, 1]$  would be the most common but not the only choice. Line-search algorithms are motivated by either the acceleration of convergence or the achievement of convergence itself in regions where the standard Newton-Raphson algorithm would diverge. Numerous methods are available to determine the value of  $\alpha_{\text{LS}}$  (Jeremic, 2001; Seifert and Schmidt, 2008; Zienkiewicz et al., 2005-2006).

Once the iteration has converged, we find the consistent tangent matrix for the global iteration using the total differential of  $\underline{r}$  and the fact that the

first entry in  $\underline{z}$  is always  $\underline{\sigma}$ :

$$\frac{d\underline{r}}{d\underline{\epsilon}^{t+\Delta t}} = \frac{\partial \underline{r}}{\partial \underline{\epsilon}^{t+\Delta t}} + \left( \frac{\partial \underline{r}}{\partial \underline{z}} \Big|_{t+\Delta t} \right) \frac{d\underline{z}}{d\underline{\epsilon}^{t+\Delta t}} = \underline{0} \quad (2.38)$$

The first entry of the solution  $d\underline{z}/d\underline{\epsilon}^{t+\Delta t}$  to the resulting linear system

$$\left( \frac{\partial \underline{r}}{\partial \underline{z}} \Big|_{t+\Delta t} \right) \frac{d\underline{z}}{d\underline{\epsilon}^{t+\Delta t}} = - \frac{\partial \underline{r}}{\partial \underline{\epsilon}^{t+\Delta t}} \quad (2.39)$$

is the sought tangent matrix  $\mathbb{C}^i$ . Thus, the tangent modulus matrix can be computed with very little extra effort based on the already known Jacobian from the local stress-update procedure and is automatically consistent with the integration algorithm chosen. The latter point is of importance for achieving the best possible convergence of the global problem (Simo and Hughes, 1998; Zienkiewicz et al., 2005-2006).

## 2.4 Thermo-mechanical coupling in OGS

When considering applications such as nuclear waste storage, CAES, etc., thermal fields influence the material behaviour of the rock salt by lowering elastic moduli and viscosity parameters or by increasing healing rates, as outlined in Nagel et al. (2017). For a general thermo-mechanical coupling, a monolithic scheme is conceivable where the coupling matrices result from the dependence of one PDE on the primary variable of the other:

$$\begin{pmatrix} \mathbb{K}_{uu} & \mathbb{K}_{uT} \\ \mathbb{K}_{Tu} & \mathbb{K}_{TT} \end{pmatrix} \begin{pmatrix} \Delta u \\ \Delta T \end{pmatrix} = \begin{pmatrix} \psi_u \\ \psi_T \end{pmatrix} \quad (2.40)$$

A monolithic THM scheme is used, for example, to simulate freezing processes in OGS-6. In general, mechanical work can be partially dissipated into heat and thus lead to local temperature changes. However, for the strain rates and boundary conditions relevant here, the coupling to temperature fields can be described as uni-directional, i.e. the temperature distribution affects the mechanical problem but not the other way around. Therefore, an efficient solution technique is to couple the thermal and mechanical initial boundary value problems (IBVP) in a staggered/partitioned fashion. In other words, with  $\rho c_p$  the volumetric isobaric heat capacity and  $\boldsymbol{\lambda}$  the thermal conductivity tensor, the PDE-system

$$\text{PDE 1: } 0 = \rho c_p \frac{\partial T}{\partial t} - \text{div}(\boldsymbol{\lambda} \text{grad} T) \quad (2.41)$$

$$\text{PDE 2: } 0 = \text{div} \boldsymbol{\sigma}(\mathbf{u}, T) + \rho \mathbf{b} = \mathbf{0} \quad (2.42)$$

is addressed by an algorithm which solves the PDE governing one of the primary variables (temperature and displacement) while keeping the other fixed and iterating until convergence. Choosing an FE residual formulation this may be illustrated by

$$\mathbb{K}_{TT} \Delta \underline{T} = \underline{\psi}_T - \underline{f}(\underline{u}) \text{ at fixed } \underline{u} \quad \leftrightarrow \quad \mathbb{K}_{uu} \Delta \underline{u} = \underline{\psi}_u - \underline{f}(\underline{T}) \text{ at fixed } \underline{T}$$

where the residuals may be modified by source term-like contributions from the other coupled processes. In case of the one way coupling considered here, i.e.  $\mathbb{K}_{Tu} = \mathbb{O}$ , the thermal IBVP is solved first, followed by the solution of the mechanical IBVP without any further iteration between both processes necessary. Details on weak forms of coupled problems and possible implementations can be found in standard references, e.g. [Lewis and Schrefler \(1998\)](#). For a detailed overview on coupling strategies in numerical simulations, we refer the reader to [Markert \(2013\)](#).

The inclusion of temperature-dependent material parameters and thermal strains will be an inherent part of the material models and algorithms used below.

## 2.5 Constitutive models

### *Thermal process*

In addition to  $\dot{h} = c_p \dot{T}$ , only one other constitutive relation is required to close Eq. (2.2) by connecting the temperature field with the heat flux vector. It is here taken simply as the linear Fourier's law:

$$\mathbf{q} = -\lambda \text{grad } T \tag{2.43}$$

### *Mechanical process*

Linear elasticity is insufficient to describe the deformation behaviour of rock salt under most practically relevant loading conditions. Viscoelastic and viscoplastic material models represent the more appropriate choice. Various material models are available in OGS for that purpose ([Kolditz et al., 2012, 2016, 2014; Nagel et al., 2017](#)), e.g. Norton and various BGR creep laws ([Hunsche and Schulze, 1994](#)), the LUBBY2 ([Heusermann et al., 1983, 2003](#)) and a variant of the Minkley material model ([Minkley et al., 2001; Minkley and Mühlbauer, 2007](#)). These models follow different concepts in calculating the creep strain rate as well as its temperature dependence:

$$\begin{aligned} \text{Norton} \quad \dot{\epsilon}_{\text{cr}} &= A \left( \frac{\sigma_{\text{eff}}}{\sigma_0} \right)^n \frac{\sigma^{\text{D}}}{\sigma_{\text{eff}}} \\ \text{BGRa} \quad \dot{\epsilon}_{\text{cr}} &= \frac{3}{2} A \left( \frac{\sigma_{\text{eff}}}{\sigma_0} \right)^n \exp \left( -\frac{Q}{RT} \right) \frac{\sigma^{\text{D}}}{\sigma_{\text{eff}}} \\ \text{BGRb} \quad \dot{\epsilon}_{\text{cr}} &= \frac{3}{2} \left[ A_1 \left( \frac{\sigma_{\text{eff}}}{\sigma_0} \right)^{n_1} \exp \left( -\frac{Q_1}{RT} \right) + \right. \\ &\quad \left. A_2 \left( \frac{\sigma_{\text{eff}}}{\sigma_0} \right)^{n_2} \exp \left( -\frac{Q_2}{RT} \right) \right] \frac{\sigma^{\text{D}}}{\sigma_{\text{eff}}} \\ \text{LUBBY2} \quad &\text{See Eqs. (2.44)–(2.51)} \\ \text{Minkley} \quad &\text{See Eqs. (2.52)–(2.61)} \end{aligned}$$

Here, we focus on the latter two which both capture stress- and temperature-dependent transient and stationary creep phases as indicated by their rheological analogues depicted in Fig. 2.3. Additionally, the Minkley model can describe plastic effects which include strain hardening and softening as well as dilatancy (Minkley et al., 2001; Minkley and Mühlbauer, 2007).

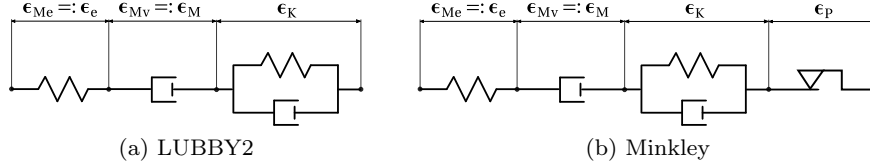


Fig. 2.3: Rheological models of the LUBBY2 and the Minkley material models.

## LUBBY2

The following set of equations describes the temperature-dependent LUBBY2 model (compare Fig. 2.3a):

$$\boldsymbol{\sigma} = K_M(e - 3\alpha_T \Delta T) \mathbf{I} + 2G_M [\boldsymbol{\epsilon}^{\text{D}} - \boldsymbol{\epsilon}_M^{\text{D}} - \boldsymbol{\epsilon}_K^{\text{D}}] \quad (2.44)$$

$$\dot{\boldsymbol{\epsilon}}_K^{\text{D}} = \frac{1}{2\eta_K} (\boldsymbol{\sigma}^{\text{D}} - 2G_K \boldsymbol{\epsilon}_K^{\text{D}}) \quad (2.45)$$

$$\dot{\boldsymbol{\epsilon}}_M^{\text{D}} = \frac{1}{2\eta_M} \boldsymbol{\sigma}^{\text{D}} \quad (2.46)$$

where the viscosities and (visco)elastic moduli are functions of both stress and strain (Böttcher et al., 2017; Du et al., 2012)

$$\eta_M = \eta_{M0} \exp(m_1 \sigma_{\text{eff}} / \sigma_0) \exp[Q(T_{\text{ref}} - T) / (RTT_{\text{ref}})] \quad (2.47)$$

$$\eta_K = \eta_{K0} \exp(m_2 \sigma_{\text{eff}} / \sigma_0) \quad (2.48)$$

$$G_K = G_{K0} \exp(m_G \sigma_{\text{eff}} / \sigma_0) \quad (2.49)$$

$$K_M = K_{M0} + m_{KT}(T - T_{\text{ref}}) \quad (2.50)$$

$$G_M = G_{M0} + m_{GT}(T - T_{\text{ref}}) \quad (2.51)$$

$$\text{with } \sigma_{\text{eff}} = \sqrt{\frac{3}{2} \sigma^{\text{D}} : \sigma^{\text{D}}}$$

For more details on the implementation, see [Nagel et al. \(2017\)](#).

### Minkley

The Minkley model as implemented in OGS and indicated in Fig. 2.3b is described by the following set of equations:

$$\boldsymbol{\sigma} = K_M(e - e_P - 3\alpha_T \Delta T) \mathbf{I} + 2G_M (\boldsymbol{\epsilon}^{\text{D}} - \boldsymbol{\epsilon}_P^{\text{D}} - \boldsymbol{\epsilon}_K^{\text{D}} - \boldsymbol{\epsilon}_M^{\text{D}}) \quad (2.52)$$

$$\dot{\boldsymbol{\epsilon}}_K^{\text{D}} = \frac{1}{2\eta_K} (\boldsymbol{\sigma}^{\text{D}} - 2G_K \boldsymbol{\epsilon}_K^{\text{D}}) \quad (2.53)$$

$$\dot{\boldsymbol{\epsilon}}_M^{\text{D}} = \frac{1}{2\eta_M} \boldsymbol{\sigma}^{\text{D}} \quad (2.54)$$

$$\dot{\boldsymbol{\epsilon}}_P^{\text{D}} = \lambda \frac{\partial G_F}{\partial \boldsymbol{\sigma}} : \boldsymbol{\mathcal{P}}^{\text{D}} \quad (2.55)$$

$$\dot{e}_P = \lambda \frac{\partial G_F}{\partial \boldsymbol{\sigma}} : \boldsymbol{\mathcal{P}}^{\text{S}} : \mathbf{I} \quad (2.56)$$

$$\dot{\boldsymbol{\epsilon}}_{P \text{ eff}} = \sqrt{\frac{2}{3}} \dot{\boldsymbol{\epsilon}}_P^{\text{D}} : \dot{\boldsymbol{\epsilon}}_P^{\text{D}} \quad (2.57)$$

$$F = 0 \quad (2.58)$$

Again, the model is characterised by stress and temperature dependencies of viscosities and elastic moduli:

$$\eta_M = \frac{\eta_{M0} \exp[Q(T_{\text{ref}} - T) / (RTT_{\text{ref}})]}{\sinh \left[ m \left( \frac{\sigma_{\text{eff}}}{\sigma_0} \right)^n \right]} \quad (2.59)$$

$$K_M = K_{M0} + m_{KT}(T - T_{\text{ref}}) \quad (2.60)$$

$$G_M = G_{M0} + m_{GT}(T - T_{\text{ref}}) \quad (2.61)$$

The yield function in Eq. (2.58) and the plastic potential required for Eqs. (2.55) and (2.56) were taken as Mohr-Coulomb types with corner smoothing:

$$F = \begin{cases} \frac{I_1}{3} \sin \phi + \sqrt{J_2} \left( \cos \theta - \frac{1}{\sqrt{3}} \sin \phi \sin \theta \right) - c \cos \phi & |\theta| < \theta_T \\ \frac{I_1}{3} \sin \phi + \sqrt{J_2} (A - B \sin 3\theta) - c \cos \phi & |\theta| \geq \theta_T \end{cases} \quad (2.62)$$

where  $c$  and  $\phi$  are the cohesion and friction angle, respectively, and

$$A = \frac{1}{3} \cos \theta_T \left[ 3 + \tan \theta_T \tan 3\theta_T + \frac{1}{\sqrt{3}} \text{sign} \theta (\tan 3\theta_T - 3 \tan \theta_T) \sin \phi \right] \quad (2.63)$$

$$B = \frac{1}{3} \frac{1}{\cos 3\theta_T} \left[ \text{sign} \theta \sin \theta_T + \frac{1}{\sqrt{3}} \sin \phi \cos \theta_T \right] \quad (2.64)$$

The plastic potential differs from the yield surface in order to more accurately estimate dilatancy, but has an analogous structure:

$$G_F = \begin{cases} \frac{I_1}{3} \sin \psi + \sqrt{J_2} \left( \cos \theta - \frac{1}{\sqrt{3}} \sin \psi \sin \theta \right) & |\theta| < \theta_T \\ \frac{I_1}{3} \sin \psi + \sqrt{J_2} (A' - B' \sin 3\theta) & |\theta| \geq \theta_T \end{cases} \quad (2.65)$$

where  $\psi$  is the dilatancy angle.  $A'$  and  $B'$  follow from Eqs. (2.63), (2.64) by substituting the friction angle with the dilatancy angle. Hardening or softening is here by a smoothly differentiable law which captures hardening, followed by softening up to a defined residual cohesion (compare also Fig. 3.8):

$$c = c_{\text{res}} + (c_0 - c_{\text{res}}) \left( 1 + A_1 \sin \frac{\epsilon_P^{\text{eff}}}{A_2} \right) \left( 1 - \frac{1}{1 + \exp[-B_1(\epsilon_P^{\text{eff}} - B_2)]} \right) \quad (2.66)$$

For more details on the implementation, see Nagel et al. (2017). The implementation of the LUBBY2 and Minkley models is verified against analytical solutions in Kolditz et al. (2016, 2014); Nagel et al. (2017).

Furthermore, a simple viscoplastic regularisation of the Perzyna type can be employed (de Borst and Heeres, 2002; Heeres et al., 2002; Wang et al., 1997): we allow stress states with  $F > 0$  by introducing a regularisation viscosity  $\eta_{\text{reg}}$  and set

$$\dot{\epsilon}_P = \frac{\langle \zeta(F) \rangle}{\eta_{\text{reg}}} \frac{\partial G_F}{\partial \boldsymbol{\sigma}} \quad (2.67)$$

A typical formulation for  $\zeta(F)$  is

$$\zeta(F) = \left( \frac{F}{C} \right)^n \quad (2.68)$$

where—to normalise  $F$ — a common choices for  $C$  is the initial yield stress. For the sake of simplicity,  $n = 1$  and  $C = G_M$  were chosen here so that the consistency condition in Eq. (2.58) is replaced by

$$\lambda\eta_{\text{reg}} = \langle \zeta(F) \rangle = \frac{\langle F \rangle}{G_M} \quad (2.69)$$

Note that a rate-independent formulation is recovered for  $\eta_{\text{reg}} = 0$ .

Viscoplastic regularisation works by a load-transfer mechanism: if deformation starts to localise in a finite band of element-width, the increase of the deformation rate in that band in conjunction with the viscous law causes a stiffening of the band and thus a preferential deformation of adjacent element layers (Niazi et al., 2013). This mechanism prevents excessive localisation. Mathematically, this rate-dependence yields a positive-definite tangent operator and hence a well-posed, regularised problem (Forest et al., 2004).

## Coupling

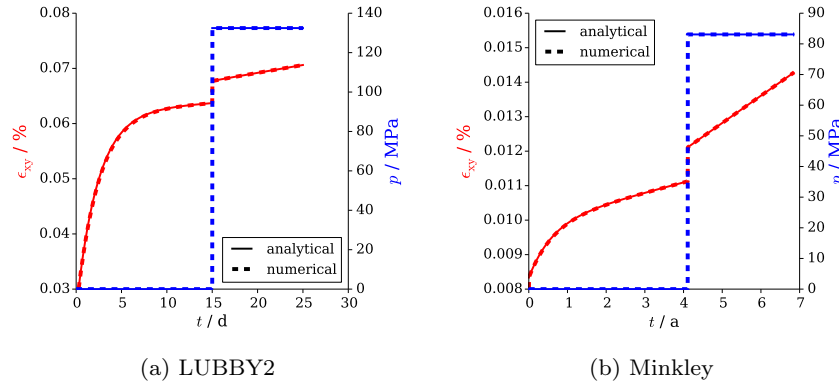


Fig. 2.4: Results of a simulated simple shear creep test for the LUBBY2 model and the Minkley model. About half-way through the test, a temperature jump was imposed causing an immediate change in the elastic response visible as a jump in the shear strain curve (red), a significant hydrostatic pressure (blue) due to isochoric confinement of the sample, as well as an increased creep rate. Details and parameters used can be found in Nagel et al. (2017).

In addition to the process coupling (compare also Section 2.4) via the effect of thermal expansion<sup>16</sup> included in Eqs. (2.44) and (2.52), the temperature field influences the material behaviour by altering the elastic and creep properties through a temperature-dependent parameterisation of the constitutive models, cf. Eqs. (2.47)–(2.51) and (2.59)–(2.61).

In a stress-controlled simple shear test, for which an analytical solution can easily be found, all effects can be illustrated, as shown in Fig. 2.4 for both the Minkley and the LUBBY2 material models.

---

<sup>16</sup> Other such coupling effects like heat of dissipation, thermoelastic or entropic effects are neglected here.

## Chapter 3

# Simulation of laboratory tests

The input files of all subsequent examples can be found on the *OGS website* <https://docs.opengeosys.org/books>. In the sequel, we will describe selected input files and keywords relevant to the specific examples. More complete and automatically updated *keyword descriptions* are available online under the link <https://svn.ufz.de/ogs/wiki/public/doc-auto> for OGS-5 and <https://doxygen.opengeosys.org/index.html> for OGS-6. Furthermore, some descriptions will be repeated for the different examples as this redundancy helps to clarify the use of the keywords.

Note that as usual in finite element codes no units are given in the input files. It is the user's responsibility to use a self-consistent unit system, e.g. the units of viscosities must match the time units (MPa d and d), the units for length and stresses need to match (MPa = N/mm<sup>2</sup> and mm), etc.

Instructions on how to *download, compile and link OGS* against external libraries can be found at <https://docs.opengeosys.org>. For *meshing and general pre-processing*, you can choose from a number of options

- ▷ OGS Data Explorer (<https://docs.opengeosys.org/docs>)
- ▷ GINA (<https://teambeam.bgr.de/my/drive#!folder=68>)
- ▷ MeshIt (Cacace and Blöcher, 2015)
- ▷ Gmsh (<http://gmsh.info/>)

For *post-processing*, the open-source software Paraview is recommended which is to be found at <http://www.paraview.org/>.

### 3.1 Non-isothermal triaxial creep test

In this example, the LUBBY2 model described in Sec. 2.5 will be used to simulate a non-isothermal triaxial creep test with inhomogeneous temperature and strain/stress fields. The boundary conditions are chosen for illustration and do not represent a particular experimental set-up.

To set up a sequentially coupled TM analysis, the two relevant processes need to be defined in the process file, see Listing 3.1.

Listing 3.1: Sequential coupling between a heat transport problem and a deformation problem in the PCS file of OGS-5.

```
#PROCESS
  $PCS_TYPE
  HEAT_TRANSPORT
#PROCESS
  $PCS_TYPE
  DEFORMATION
#STOP
```

### *Geometry and boundary conditions*

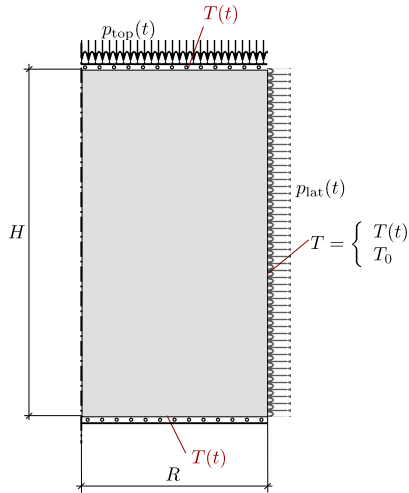


Fig. 3.1: A cylindrical sample of radius  $R = 30$  mm and height  $H = 120$  mm is assumed to rest on a frictionless platen. The top of the sample is loaded by a vertical traction (i.e. not by a rigid platen so that bending modes may occur), while a confining pressure  $p$  is imposed on the lateral surface. The top and bottom of the sample can be heated while the lateral surface is either heated in the same way as the other platens (case 1) or is maintained at ambient temperature (case 2).

The cylindrical sample (Fig. 3.1) is modelled using axisymmetry, i.e. a 3D problem is simulated using a 2D mesh. The mesh file includes an appropriate keyword (Listing 3.2).

Listing 3.2: Making a 2D mesh axisymmetric in the MSH file. Note that ”;” comments a line in an OGS-5 input file.

```
#FEM_MSH
$AXISYMMETRY
$NODES
341
;num      x      y      z
0         0      0      0
1         7.5    0      0
...
$ELEMENTS
300
;num      mat_id  el_type  node_list
0         0      quad     0 1 2 3
1         0      quad     3 2 4 5
...
```

The boundary conditions indicated in Fig. 3.1 are given by a series of ramp-and-hold profiles (compare Fig. 3.2):

$$\begin{aligned}
r = 0 : \quad & \text{symmetry} & \forall t \in [0, t_{\text{end}}] \\
r = R : \quad & \sigma_{rr}(t) = -p_{\text{lat}} \left( \frac{t - \langle t - t_0 \rangle}{t_0} \right) & \forall t \in [0, t_{\text{end}}] \\
& T(t) = \begin{cases} T_0 + \Delta T \left( \frac{\langle t - t_1 \rangle - \langle t - t_2 \rangle}{t_2 - t_1} \right) \\ T_0 \end{cases} & \forall t \in [0, t_{\text{end}}] \\
z = 0 : \quad & u_z(t) = 0 & \forall t \in [0, t_{\text{end}}] \\
& T(t) = T_0 + \Delta T \left( \frac{\langle t - t_1 \rangle - \langle t - t_2 \rangle}{t_2 - t_1} \right) & \forall t \in [0, t_{\text{end}}] \\
z = H : \quad & \sigma_{zz}(t) = -p_{\text{top}} \left( \frac{t - \langle t - t_0 \rangle}{t_0} \right) & \forall t \in [0, t_{\text{end}}] \\
& T(t) = T_0 + \Delta T \left( \frac{\langle t - t_1 \rangle - \langle t - t_2 \rangle}{t_2 - t_1} \right) & \forall t \in [0, t_{\text{end}}]
\end{aligned}$$

where  $\langle \rangle$  are the Macauley brackets. The values for the constants appearing in the boundary conditions are given in Table 3.1.

$p_{\text{lat}}$ / MPa	$p_{\text{top}}$ / MPa	$\Delta T$ / K	$t_0$ / d	$t_1$ / d	$t_2$ / d
5	12	50	0.05	20	21

Table 3.1: Parameterisation of boundary conditions.

Initial conditions are given in the \*ic file in OGS-5, Dirichlet boundary conditions in the BC file and Neumann boundary conditions in the ST file. All of them are assigned to geometric entities defined in the GLI file such as points, polylines, surfaces or the entire domain. We leave it to the reader to

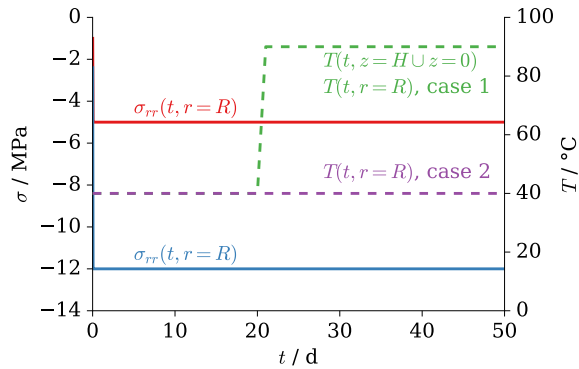


Fig. 3.2: Radial confining stress, axial stress and temperature curves applied as boundary conditions via a series of ramp-and-hold curves in the triaxial test with parameters from Table 3.1.

check the GLI file for this example<sup>17</sup> in which the polylines named BOTTOM, TOP, OUTER and INNER define the bottom, top and outer surfaces as well as the axis of symmetry for the axisymmetric mesh.

The only initial condition necessary here defines the initial temperature.

Listing 3.3: Initial condition for the temperature in the IC file.

```
#INITIAL_CONDITION
$PCS_TYPE
HEAT_TRANSPORT
$PRIMARY_VARIABLE
TEMPERATURE1
$GEO_TYPE
DOMAIN
$DIS_TYPE
CONSTANT 313
#STOP
```

As seen in Listing 3.3, the heat transport process is assigned an initial condition for its primary variable temperature<sup>18</sup> on the entire solution domain of a constant value of 313 K.

The syntax to define boundary conditions is very similar. Here, we select two examples from the BC file.

<sup>17</sup> More information under <https://svn.ufz.de/ogs/wiki/public/doc-auto>.

<sup>18</sup> The number indicates the possibility to account for local thermal non-equilibrium and hence several temperatures at a given point.

Listing 3.4: Selected Dirichlet boundary conditions defined in the BC file.

```

#BOUNDARY_CONDITION
$PCS_TYPE
  DEFORMATION
$PRIMARY_VARIABLE
  DISPLACEMENT_Y1
$GEO_TYPE
  POLYLINE BOTTOM
$DIS_TYPE
  CONSTANT 0

#BOUNDARY_CONDITION
$PCS_TYPE
  HEAT_TRANSPORT
$PRIMARY_VARIABLE
  TEMPERATURE1
$GEO_TYPE
  POLYLINE TOP
$DIS_TYPE
  CONSTANT 313
$TIM_TYPE
  CURVE 3

...
#STOP

```

In Listing 3.4, the constraint on the vertical displacement at the sample bottom ( $z = 0$ ) is shown along with a temperature boundary condition at the sample top. The distribution type (`$DIS_TYPE`) `CONSTANT` refers to the spatial homogeneity along the geometrical entity, while the time type (`$TIM_TYPE`) in the temperature boundary condition indicates a multiplicative scaling of the given value of 313 K by the time-dependent curve number 3, which we shall explain shortly, in order to define the boundary condition  $T(t)$ , see Figs. 3.1 and 3.2.

Source terms are usually defined in balance equations as supply terms per unit volume of a domain, while Neumann boundary conditions arise in the weak form from surface fluxes associated with the balanced quantity. While this distinction is strictly adhered to in OGS-6, Neumann boundary conditions are defined in OGS-5 input files under the tag source term and are assigned the distribution type `CONSTANT_NEUMANN`.

Listing 3.5: Selected Neumann boundary condition defined in the ST file.

```

#SOURCE_TERM
$PCS_TYPE
  DEFORMATION
$PRIMARY_VARIABLE
  DISPLACEMENT_X1
$GEO_TYPE
  POLYLINE OUTER
$DIS_TYPE
  CONSTANT_NEUMANN -5.0
$TIM_TYPE
  CURVE 1
...
#STOP

```

The confining pressure defined at  $r = R$  in Listing 3.5 carries a negative sign as the traction vector points against the positive radial coordinate direction. It is again scaled by a time-dependent curve (Fig. 3.2).

These curves are given in the RFD file and automatically numbered consecutively starting at 1.

Listing 3.6: Selected Dirichlet boundary condition defined in the ST file.

```

;confining pressure
#CURVES
; time      factor
  0.0       0.0
  0.05      1.0
  1.e6      1.0

;top pressure
#CURVES
  0.0       0.0
  0.05      1.0
  1.e6      1.0

;temperature
#CURVES
  0.00e+00  1.0
  20        1.0
  21        1.16
  1.e6      1.16
#STOP

```

The value pairs defined in these curves (Listing 3.6) define at which point in time which factor is multiplied to the boundary condition to obtain its current value. In between the time points, OGS interpolates linearly creating piecewise linear functions.

## Material properties

$G_{M0} / \text{MPa}$	$K_{M0} / \text{MPa}$	$\eta_{M0} / \text{MPa d}$	$G_{K0} / \text{MPa}$	$\eta_{K0} / \text{MPa d}$
$9.54 \cdot 10^3$	$2.78 \cdot 10^4$	$4.03 \cdot 10^7$	$6.27 \cdot 10^4$	$1.66 \cdot 10^5$
$m_1 / \text{MPa}^{-1}$	$m_2 / \text{MPa}^{-1}$	$m_G / \text{MPa}^{-1}$	$m_{GT} / \text{MPa K}^{-1}$	$m_{KT} / \text{MPa K}^{-1}$
-0.327	-0.267	-0.254	-21.141	-25.265
$Q / \text{J mol}^{-1}$	$T_{\text{ref}} / \text{K}$	$\alpha_T / \text{K}^{-1}$	$c_p / \text{J kg}^{-1} \text{K}^{-1}$	$\lambda / \text{W mm}^{-1} \text{K}^{-1}$
$1.6 \cdot 10^4$	313	$2.8 \cdot 10^{-5}$	920	648
$\rho / \text{kg mm}^3$	$T_{\text{ref}} / \text{K}$	$\alpha_T / \text{K}^{-1}$		
$2.04 \cdot 10^{-6}$	313	$2.8 \cdot 10^{-5}$		

Table 3.2: Temperature-independent material parameters for the LUBBY2 model; Eqs. (2.44)–(2.51). Parameters from Heusermann et al. (1983, 2003). Parameters describing the temperature dependence of the elastic properties taken from reference (Sriapai et al., 2012), and of the stationary creep rate following (Du et al., 2012).

The above material properties are given in the solid properties (MSP) file.

Listing 3.7: The solid properties (MSP) file. Note that there are *no manual line breaks* (indicated here by `\\`) in the actual file.

```
#SOLID_PROPERTIES
$DENSITY
1 2.04e-06
$CREEP_BURGERS
;G_K0,      m_G,      eta_K0, m_2,      G_M0,      K_M0,      \\
eta_M0,      m_1,      m_GT,      m_KT,      T_ref B Q
6.2667e4 -2.54e-1 1.66e5 -2.67e-1 9.5420E+003 2.7798E+004 \\
4.03e7 -3.27e-1 -21.1405 -25.265 313 1.0 16000
$THERMAL
EXPANSION 2.8e-05
CAPACITY
1 920
CONDUCTIVITY
1 648
$GRAVITY_CONSTANT
0.0
#STOP
```

The key word `$CREEP_BURGERS` invokes the LUBBY2 formulation. The parameter names and values given in Listing 3.7 correspond to Table 3.2.

Note that the order of the values is fixed and must not be altered. The first number for `$DENSITY`, `CAPACITY` and `CONDUCTIVITY` indicates a particular functional relationship, 1 meaning simply a constant value which is then given as the second number. The final keyword indicates that gravity has been switched off in this example.

Without showing the respective input files it should be mentioned that two more files are necessary to run a TM analysis in OGS-5: the fluid properties (MFP) file must define basic thermal and hydraulic properties of the pore fluid. Even though no flow analysis is performed as would be done for a full THM scenario, this feature enables the simulation of a porous medium with effective thermal properties, when the presence of the fluid has no mechanical consequences but fluid properties can follow their own equations of state. Thus, solid and fluid properties such as thermal conductivity may follow their own temperature-dependent constitutive functions, and the effective properties are determined by a homogenisation step.

The MMP file then defines certain properties of the solid–fluid mixture, i.e. the porous medium. Among others, it defines the porosity of the solid. Here, the porosity is given as 0, such that the fluid properties become irrelevant for the thermal analysis due to the volume fraction-based averaging process.

## Numerical settings

Listing 3.8: Numerical settings in the NUM file.

```
#NUMERICS
$PCS_TYPE
HEAT_TRANSPORT
$LINEAR_SOLVER
; method error_tolerance max_iterations theta precondition storage
; 2 5 1.0e-14 5000 1.0 100 4 ; internal
; 4 5 1.0e-18 15000 1.0 2 4 ; LIS
805 6 1.0e-15 15000 1.0 2 4 ; PARDISO
$ELE_GAUSS_POINTS
3

#NUMERICS
$PCS_TYPE
DEFORMATION
$LINEAR_SOLVER
; method error_tolerance max_iterations theta precondition storage
; 2 5 1.0e-14 5000 1.0 100 4 ; internal
; 4 5 1.0e-18 15000 1.0 2 4 ; LIS
805 6 1.0e-15 15000 1.0 2 4 ; PARDISOSO
$ELE_GAUSS_POINTS
3

$NON_LINEAR_ITERATIONS
; method error_type max_iterations relaxation convergence_control
NEWTON BNORM 20 0.0 1.0e-6

$ADDITIONAL_NEWTON_TOLERANCES
1.e+10 1.0e-3 1.0e+10

$PLASTICITY_TOLERANCE
1.e-14

#STOP
```

Two sets of numerical settings are included in the NUM file (Listing 3.8): The first for heat transport, the second for the mechanical process. Depending on how you build OGS, different linear solvers and solver libraries are available. If linking against the Intel MKL library<sup>19</sup>, the direct Pardiso solver can be used. It is invoked by the line starting with 805. If linking against the Lis iterative solver library<sup>20</sup>, the line starting with 4 is appropriate. The settings in this example invoke the BiCGStab solver with an ILU preconditioner. One can also use internal OGS solvers (first line starting with a 2) without linking against third party solver libraries; however, we recommend one of the former options. Both MKL Pardiso and Lis make use of OpenMP: by changing the environment variable `OMP_NUM_THREADS` you can determine how many threads are to be used in parallel for solving the linear system.

By including `$NON_LINEAR_ITERATIONS`, OGS performs a Newton-Raphson iterations to obtain the displacement solution where the user typically sets

<sup>19</sup> <https://software.intel.com/en-us/intel-mkl>

<sup>20</sup> <http://www.ssisc.org/lis/>

the maximum number of iterations (here 20) and a tolerance value for convergence control (here  $1 \cdot 10^{-6}$ ). This value corresponds to a relative residual norm (compare Eq. (2.25)). Should one require other convergence settings, the keyword `$ADDITIONAL_NEWTON_TOLERANCES` allows the user to set tolerances for (in that order) the norms of the absolute residual, the absolute displacement increment and the relative displacement increment. A global Newton loop converges only if all tolerance settings are met. Here, the absolute displacement increment and the relative residual are checked while the high values given for the remaining criteria render them irrelevant. Note that absolute norms are sensitive to the dimension (units) of the problem studied, while relative norms are not. In some cases, such as load-free or idling phases, absolute criteria may be required for convergence rather than relative criteria. Which tolerance values to choose thus may depend on problem dimension, time stepping, non-linearity, desired accuracy in relation to computing time, and a number of other factors. If no experience for a particular problem type is available, the effect of tolerance settings on the results must be studied in order to determine suitable values. For more information see also [Bathe \(2014\)](#); [Zienkiewicz et al. \(2005-2006\)](#) and others.

Finally, the keyword `$PLASTICITY_TOLERANCE` specifies the tolerance for the norm of the residual from the local stress-update algorithm, see Eq. (2.36). Note that the precision of the local solution directly affects both precision and convergence of the global problem.

## *Time stepping*

Listing 3.9: Time stepping defined in the TIM file.

```
#TIME_STEPPING
$PCS_TYPE
  DEFORMATION
$TIME_STEPS
  20 0.005
  9  0.1
  18 0.5
  10 1.0
  10 0.1
  18 0.5
  20 1.0
  10 5.0
$TIME_END
  120.0
$TIME_START
  0
#STOP
```

Fixed time stepping is chosen for this problem. The TIM file (Listing 3.9) contains a list of (number of time steps; time-step length)-pairs as well as the

end time. The simulation stops as soon as either all time steps are used up or once the end time is reached. One time-stepping entry is sufficient here, as equal time-stepping schemes and widths were chosen for both subproblems.

## Output

Listing 3.10: Output quantities defined in the OUT file.

```
#OUTPUT
$NOD_VALUES
  DISPLACEMENT_X1
  DISPLACEMENT_Y1
  STRESS_XX
  STRESS_XY
  STRESS_YY
  STRESS_ZZ
  STRAIN_XX
  STRAIN_XY
  STRAIN_YY
  STRAIN_ZZ
  TEMPERATURE1
$GEO_TYPE
  DOMAIN
$DAT_TYPE
  PVD
$TIM_TYPE
  STEPS 1
#STOP
```

Several sets of output tasks can be defined simultaneously for a simulation in the OUT file (Listing 3.10). They can have different file formats, different frequencies; they can be defined for separate processes and on different geometric entities. Here, we output some standard quantities in the nodes of a finite element mesh<sup>21</sup>, namely on the entire domain. The output is performed after every time step (STEPS 1) and in ParaViewData format. The latter implies the creation of a series of VTU files for each time step with their time sequence information collected in the PVD file.

Note in passing the following convention for axisymmetric analyses followed in OGS-5: as the mesh-file is set up in  $(x, y)$  coordinates corresponding to the cylinder coordinates  $(r, z)$ , displacements in these directions are referred to as  $x$  and  $y$ . For stress and strain output, the following convention is used:  $(x, y, z) \leftrightarrow (r, \phi, z)$ .

<sup>21</sup> Integration point quantities such as stresses and strains are extrapolated to the nodes for output.

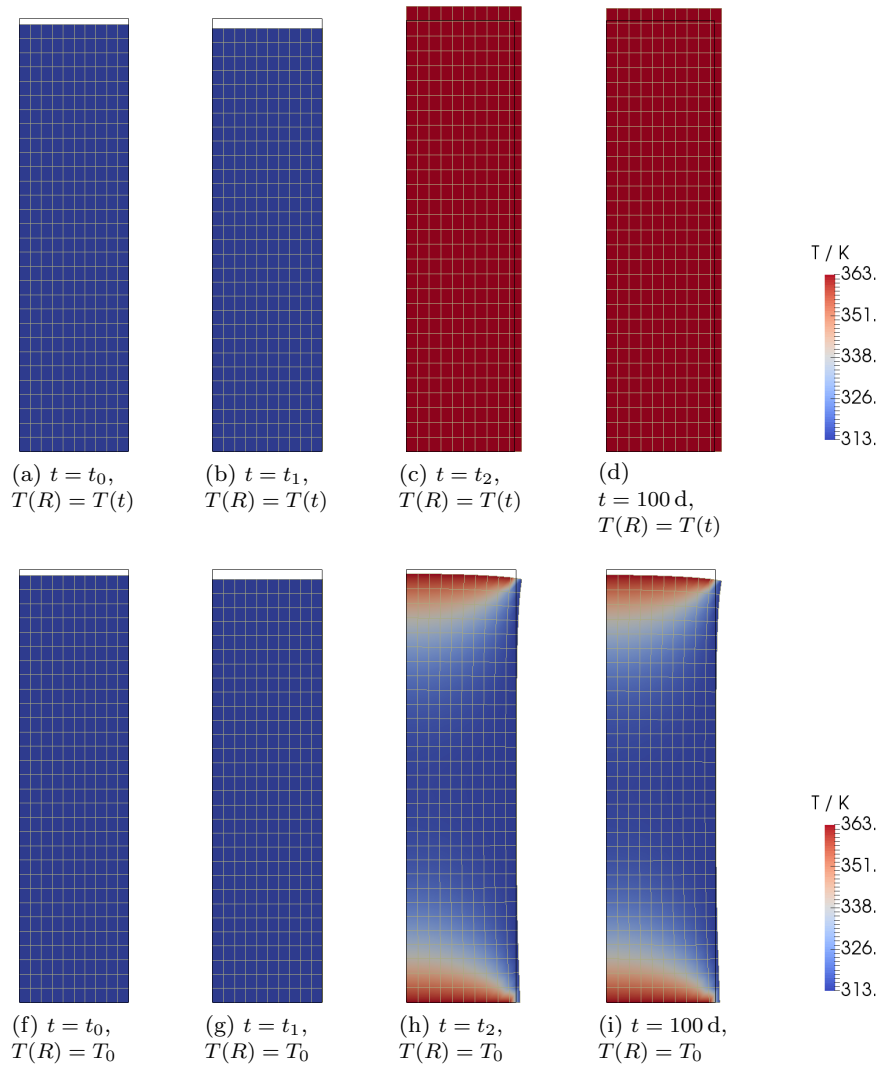
*Simulation results*

Fig. 3.3: Triaxial creep test simulated using the LUBBY2 material model with either a homogeneous temperature field (top row) or a heterogeneous temperature field (bottom row). The mesh is plotted in the deformed state, where displacements have been magnified by a factor of 40. The black box shows the undeformed state for comparison.

At the end of loading ( $t = t_0$ ) the sample is compressed mainly elastically. Following the top right node, i.e. the perimeter of the sample top ("the top edge"), this step is apparent by the rapid axial displacement in Fig. 3.4. During the subsequent creep phase, the two characteristic creep stages are observed: a primary, transient creep phase with a decreasing rate lasting roughly 10 days, followed by a secondary, stationary creep phase at constant rate. The behaviour in the subsequent stages differs strongly depending on the lateral temperature boundary condition (Fig. 3.3).

In case 1, where the lateral boundary is subjected to the same temperature boundary condition as the top and bottom boundaries, i.e.  $T(R) = T(t)$ , a homogeneous temperature field develops after the heating process. The temperature increase of 50 K throughout the sample leads to a large and homogeneous volumetric expansion. The sample increases significantly in both height and radius (Fig. 3.3c) and does so homogeneously. Because the volume increase is homogeneous, the shear stress state does not change. Hence, the subsequent creep phase remains entirely stationary albeit at a higher rate due to the temperature-induced viscosity decrease throughout the sample (Fig. 3.4).

In case 2, the lateral boundary is maintained at the initial temperature,  $T(R) = T_0$ , leading to the development of a highly heterogeneous temperature field (Fig. 3.3). Thermal expansion is limited to the vicinity of the top and bottom surfaces, resulting in a much lower overall volume increase. Furthermore, the differential thermal expansion leads to a distortion of the sample's geometry (Figs. 3.3h and 3.3i). This affects the deviatoric stress state, initiating a small primary creep phase after the heating step (Fig. 3.4). Because the sample remains cool in large parts, the average viscosity increase is lower compared to case 1 and the increase in the compression rate is accordingly less significant.

**TASK:** The user can experiment with the interplay of boundary conditions, time curves, time stepping, mesh density, and numerical settings to develop a feel for the right settings. Analytical solutions are one possibility to quantify errors depending on the discretisation, convergence criteria etc. Possible test cases can be found in Nagel et al. (2017).

Another possible variation that we leave for practice is the modification of the boundary conditions to no-slip conditions ( $u_r(z = 0) = u_r(z = H) = 0$ ) to observe the typical barreling of the samples (compare also Kolditz et al. (2016)).

For convenience, three different mesh files were added to the input file collection (Fig. 3.5) but others are of course possible. Note, if the dimensions of the mesh file are changed, the geometry in the GLI file must be adapted accordingly.

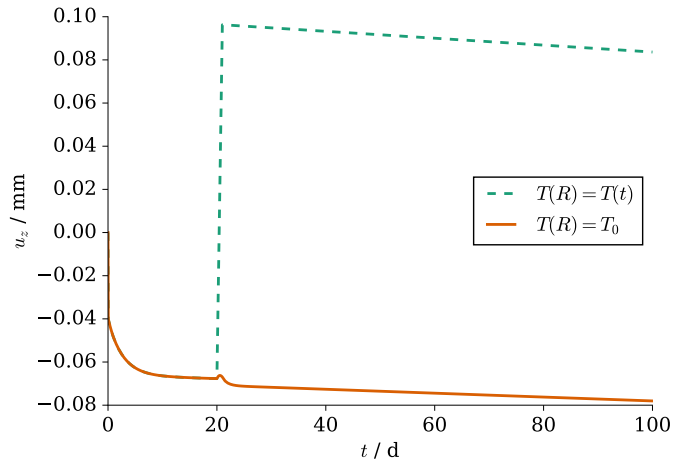


Fig. 3.4: Axial displacement of the top left node, i.e. the point (or line) located at  $r = R$  and  $z = H$ .

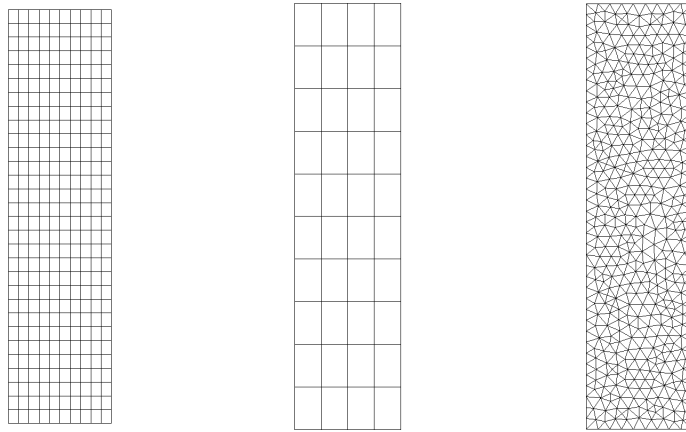


Fig. 3.5: Three meshes are available for the simulation.

### 3.2 Triaxial test with plasticity

In this example, the Minkley model described in Sec. 2.5 will be used to simulate an isothermal multi-step triaxial compression test with relaxation phases. The material behaviour is significantly more non-linear than the previous example. As the test is isothermal, the PCS file simply contains the DEFORMATION process. No boundary or initial conditions need to be defined for the temperature field and no MFP file is necessary.

### Geometry and boundary conditions

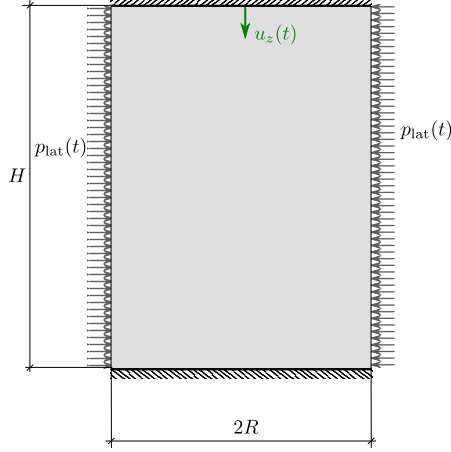


Fig. 3.6: A cylindrical sample of radius  $R = 30$  mm and height  $H = 120$  mm is assumed to rest between two high-friction platens (“glued contact”). The top of the sample is loaded by a vertical displacement  $u_z(t)$ , while a confining pressure  $p_{\text{lat}}(t)$  is imposed on the lateral surface.

The boundary conditions plotted in Fig. 3.7 are  $\forall t \in [0, t_{\text{end}}]$ :

$$\begin{aligned}
 r = R : \sigma_{rr}(t) &= -p_1 \left( \frac{t - \langle t - t_0 \rangle}{t_0} \right) - \Delta p \left( \frac{\langle t - t_5 \rangle - \langle t - t_6 \rangle}{t_6 - t_5} \right) \\
 z = 0 : u_z &= 0 \\
 &u_r = 0 \\
 z = H : u_r &= 0 \\
 u_z(t) &= -u_0 \left( \frac{\langle t - t_0 \rangle - \langle t - t_1 \rangle}{t_1 - t_0} \right) + \Delta u_1 \left( \frac{\langle t - t_2 \rangle - \langle t - t_3 \rangle}{t_3 - t_2} \right) \\
 &\quad - \Delta u_1 \left( \frac{\langle t - t_4 \rangle - \langle t - t_5 \rangle}{t_5 - t_4} \right) - \Delta u_2 \left( \frac{\langle t - t_6 \rangle - \langle t - t_7 \rangle}{t_7 - t_6} \right)
 \end{aligned}$$

where  $\langle \rangle$  are the Macauley brackets. The values for the constants appearing in the boundary conditions are given in Table 3.3.

The geometric input is similar to the previous example. However, no axisymmetry condition is applied in this case to not enforce symmetry constraints on shear band formation. Hence, a two-dimensional mesh is used in conjunction with the plane strain assumption. This also implies a change in boundary conditions on the “left” polyline: it no longer represents a symmetry axis ( $u_r = 0$ ) but the opposing lateral boundary. As such it needs to be assigned the appropriate traction boundary condition.

In summary, a series of ramp-and-hold profiles with the following characteristics is performed, compare Fig. 3.7:

- Application of a radial confining stress of  $-4$  MPa within 2 days.
- Application of  $-0.12\%$  axial strain within 2 days.

- Hold all boundary conditions for 100 days.
- Reduction of the axial strain to  $-0.09\%$  within 2 days.
- Hold all boundary conditions for 100 days.
- Increase axial strain back to  $-0.12\%$  within 2 days.
- Increase radial confining stress to  $-8\text{ MPa}$  within 2 days.
- Increase axial strain to  $-0.32\%$  within 2 days.

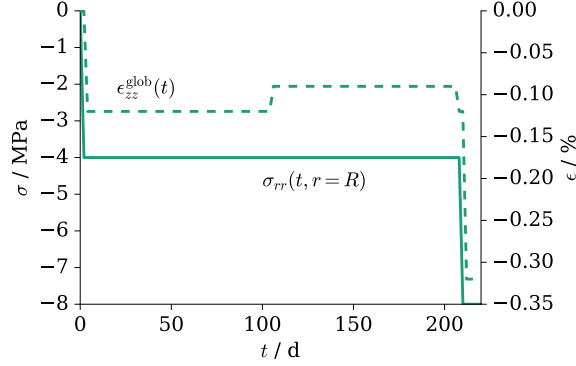


Fig. 3.7: Radial confining stress and global axial strain applied as boundary conditions as a series of ramp-and-hold curves in the triaxial test with parameters from Table 3.3.

$p_1 / \text{MPa}$	$\Delta p / \text{MPa}$	$u_0 / \text{mm}$	$\Delta u_1 / \text{mm}$	$\Delta u_2 / \text{mm}$	$t_0 / \text{d}$
4	4	0.144	0.036	0.24	2

$t_1 / \text{d}$	$t_2 / \text{d}$	$t_3 / \text{d}$	$t_4 / \text{d}$	$t_5 / \text{d}$	$t_6 / \text{d}$	$t_7 / \text{d}$
4	104	106	206	208	210	212

Table 3.3: Parameterisation of boundary conditions.

### *Material properties*

The material parameters were chosen as given in Table 3.4. In particular, the corresponding hardening/softening via the cohesion depending on plastic strain is plotted in Fig. 3.8.

$G_M / \text{MPa}$	$K_M / \text{MPa}$	$\eta_{M0} / \text{MPa}\cdot\text{d}$	$G_{K0} / \text{MPa}$	$\eta_{K0} / \text{MPa}\cdot\text{d}$	$m / \text{MPa}^{-n}$
$1.2\cdot 10^4$	$1.8\cdot 10^4$	$10.0\cdot 10^{10}$	$6.3\cdot 10^4$	$1.4\cdot 10^6$	4.9
$n$	$c_0 / \text{MPa}$	$c_{\text{res}} / \text{MPa}$	$\phi / ^\circ$	$\psi / ^\circ$	$\eta_{\text{reg}} / \text{d}$
0.33	1.6	0.5	30.0	10.0	0.05/0.01/0.001
$A_1$	$A_2$	$B_1$	$B_2$	$\theta_T / ^\circ$	
0.4	$10^{-3}$	$3\cdot 10^3$	$4\cdot 10^{-3}$	28	

Table 3.4: Material parameters for the Minkley model; Eqs. (2.52)–(2.59) and (2.66). Information on parameter identification can be found in Hampel et al. (2010). The parameters of the hardening/softening law were arbitrarily chosen for illustration.

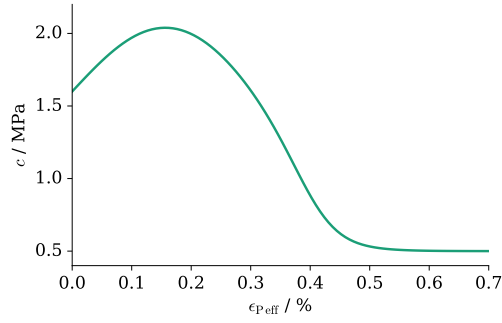


Fig. 3.8: The hardening/softening law from Eq. (2.66) with the parameters from Table 3.4.

The above material properties are given in the solid properties (MSP) file.

Listing 3.11: The solid properties (MSP) file invoking the Minkley material model. Note that there are *no manual line breaks* (indicated here by `\\`) in the actual file.

```
#SOLID_PROPERTIES
$DENSITY
1 2.2E-6
$CREEP_MINKLEY
;G_K, mu_K, G_M, K_M, eta_M0, m_vM, n_vM, c0, c_res, phi, psi, \\
thetaT, eta_reg, m_TG, m_TK, T_ref, B, Q, A1, A2, B1, B2
63.e3 14.e5 12.e3 18.e3 10.e10 4.9 0.33 1.6 0.5 20. 5. \\
28. 0.01 0.0 0.0 313. 1. 0. .4 1.e-3 3.e3 4.e-3
$GRAVITY_CONSTANT
0.0
#STOP
```

The key word `$CREEP_MINKLEY` invokes the Minkley formulation. The parameter names and values given in Listing 3.11 correspond to Table 3.4. Note that the order of the values is fixed and must not be altered. The source code may, however, change to include more or other parameters, potentially altering read functions. Thus, checking the code documentation and comments is the safest way to keeping up-to-date input.

## Numerics

Softening material behaviour is challenging for convergence. The interplay between time-step size, hardening/softening parameters in Eq. (2.66), the regularisation method (non-local, gradient, viscous) and parameters etc. is very tight. The convergence behaviour can be drastically improved and the time-step sizes increased when employing a line-search method.

**TASK:** The code version supplied with this tutorial does not feature a line-search algorithm in the local stress-update procedure. A quick sampling of the kind

$$\alpha_{LS} = \operatorname{argmin} \left\| r \left( \underline{z}^j + \alpha \Delta \underline{z}^{j+1} \right) \right\| \quad \forall \alpha \in (0, 1] \quad (3.1)$$

can, however, be readily implemented for given  $\underline{z}^j$  and  $\Delta \underline{z}^{j+1}$ . The interested user can try to implement such a scheme themselves. The function `LocalNewtonMinkley` in the source file `rf_msp_new.cpp` is a good starting point.

In the subsequent examples, a viscoplastic approach is used to aid convergence and regularise the problem in the presence of softening-induced local-

isation phenomena. In the sequel, we will compare results obtained for three different values of  $\eta_{\text{reg}}$  and discuss associated limitations of the approach.

### 3.2.1 Results

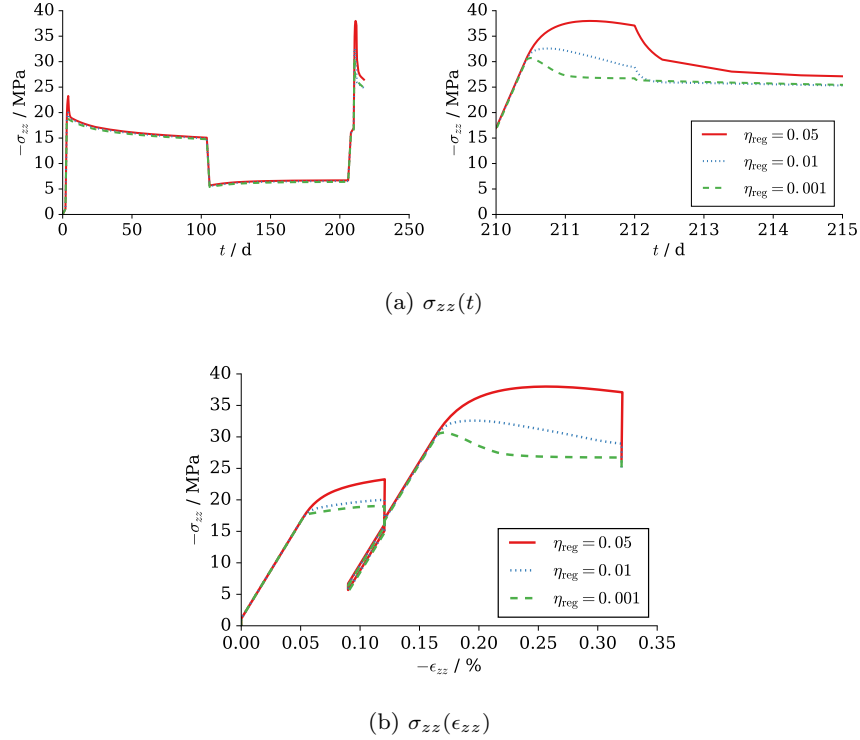


Fig. 3.9: Stress-time and stress-strain curves for the triaxial compression test using the Minkley material model. Plotted quantities represent the average over the entire specimen.

Rate-dependent material effects which are mainly due to the Burgers-part of the rheological model are visible in the stress-strain curve plotted in the left part of Fig. 3.9a. After compressive loading stops at day 4, stress relaxation with a decreasing compressive axial stress takes place. Similarly, after partial unloading at day 106, stress relaxation occurs with an increasing compressive axial stress. These relaxation phases correspond to the vertical lines at 0.12% and 0.09% axial compressive strain in the stress-strain diagramme, Fig. 3.9b.

Another rate-dependent effect is visible during plastic loading itself and has its origin in the viscoplastic regularisation performed in Eq. (2.67), see the right part of Fig. 3.9a and Fig. 3.9b. The onset of plastic loading is visible in Fig. 3.9b by the sudden change in slope around 0.05 % as well as 0.16 % axial compression. Plasticity during re-loading occurs at a much higher stress level of around 30 MPa compared to around 17 MPa during the initial loading phase. This is due to the dependence of the yield function on hydrostatic stress and the fact that during re-loading the radial confining stress has been doubled.

Hardening is visible during the initial plastic loading. The overstresses induced are only of minor importance in this phase except for the highest viscosity ( $\eta_{\text{reg}} = 0.05$  d). In the second plastic phase (re-loading), the transition to a softening material behaviour becomes apparent. In the nearly rate-independent solution ( $\eta_{\text{reg}} = 0.001$  d), the stress-strain curve qualitatively reflects the behaviour of the hardening/softening law (compare Figs. 3.9b and 3.8). Due to the tendency towards localisation in the softening regime, the viscous overstresses induced by Eq. (2.67) become more significant depending on the value of the viscosity  $\eta_{\text{reg}}$ . Once the second compression phase is terminated at day 212, the viscous overstress relaxes (right part of Fig. 3.9a and Fig. 3.9b) until the final stress values are quite similar at day 215 with the exception again of the highest viscosity.

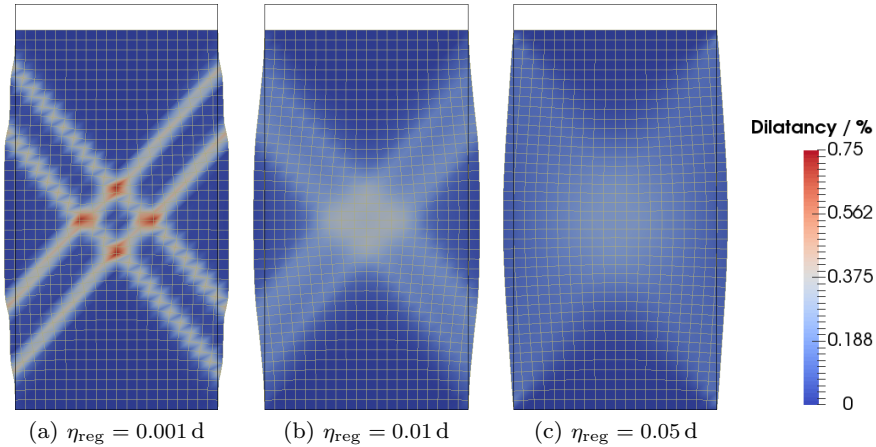


Fig. 3.10: Dilatancy for a triaxial test simulated with the Minkley material model. Deformed contour obtained by the displacement field scaled by a factor of 20.

Viscoplastic regularisation does thus not only help to treat localisation phenomena, but introduces an additional rate-dependence which alters the

stress–strain(-rate) behaviour of the material and affects the peak stresses as well as the total dissipated energy. The efficacy and consequences of the approach depend on the manner in which boundary conditions are applied, particularly the loading rate. Taken together, maintaining physical results in terms of shear-band width, stress–strain behaviour, dissipated energy, etc. for different sets of boundary conditions as well as a numerically favourable setting is a challenging task and sometimes impossible. As an alternative, micropolar, non-local or gradient-based approaches may be considered as more suitable choices for regularising softening problems.

We now compare the spatial distribution of field variables associated with the plastic response at the end of the simulation (day 215).

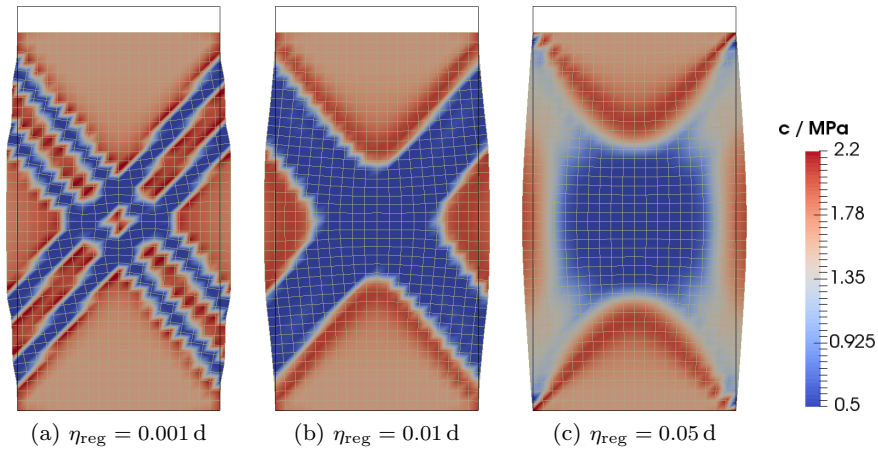


Fig. 3.11: Cohesion for a triaxial test simulated with the Minkley material model. Deformed contour obtained by the displacement field scaled by a factor of 20.

Shear-band width as well as the peak values of the dilatancy differs for the three simulations (Fig. 3.10). The overall angular pattern of the shear bands is qualitatively consistent between the simulations. The tendency for localisation is clearly visible in the quasi rate-independent simulation (Fig. 3.10a). The locally highest dilatancy values occur at the intersection between the opposing bands. Higher values for  $\eta_{\text{reg}}$  lead to an increasing spreading-out of the plastic zone accompanied by significantly lower peak dilatancy values. The overall sample develops a barrel-like shape with a smoother outer contour in the highly viscoplastic cases.

In all simulations, the samples have softened significantly (Fig. 3.11), i.e. the cohesion reached the residual value defined in the input file ( $c_{\text{res}} = 0.5 \text{ MPa}$ ). Adjacent to the softened regions, the material is still in its peak-

hardening state. The viscoplastic simulation shows a smoother distribution of the cohesion field. The simulation with the highest viscosity value has developed no fully softened cross-section but has softened maximally only in its central core (Fig. 3.11c, right). In contrast, two ( $\eta_{reg} = 0.01$  d, Fig.3.11b) respectively four ( $\eta_{reg} = 0.001$  d, Fig.3.11a) continuous bands with only residual cohesion have developed in the other simulations.

Fig. 3.12 shows the resulting shear-band width, cohesion and dilatancy field when using a significantly refined mesh consisting of 13,041 nodes instead of 861 nodes. One can observe that the viscoplastic regularisation using  $\eta_{reg} = 0.01$  d achieved a mesh-independent final result.

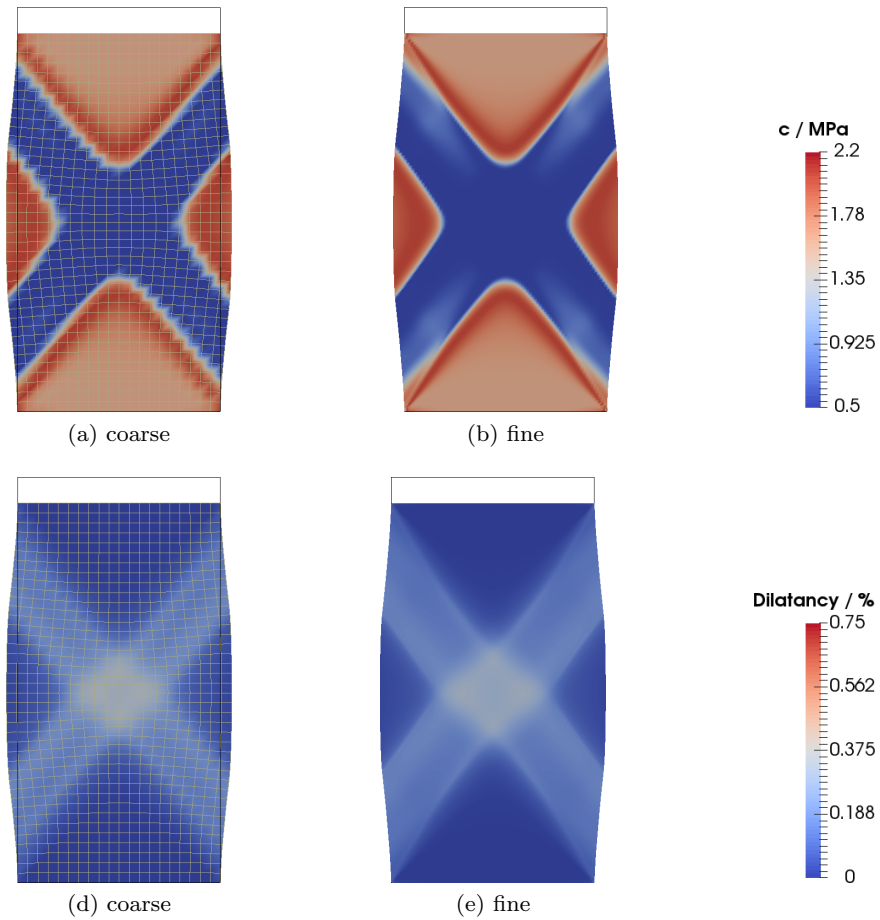


Fig. 3.12: Comparison of the resulting cohesion and dilatancy fields when a coarse (861 nodes) and a fine mesh (13041 nodes) are used. Deformed contour obtained by the displacement field scaled by a factor of 20.

Similarly, the global stress–strain response for both meshes corresponds well (Fig. 3.13).

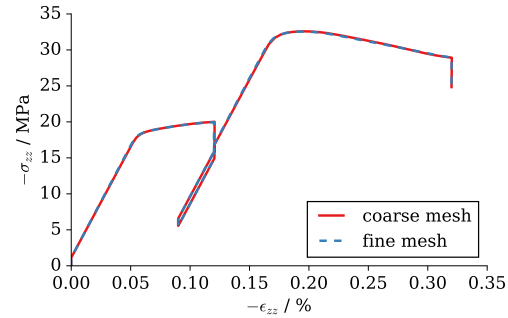


Fig. 3.13: Comparison of the resulting stress–strain curve when a coarse (861 nodes) and a fine mesh (13041 nodes) are used ( $\eta_{\text{reg}} = 0.01$  d).

**TASK:** What is the influence of mesh-density in this example when using other values for  $\eta_{\text{reg}}$ ? Use coarser and finer meshes to observe the behaviour of localisation. Try to find suitable values for  $\eta_{\text{reg}}$  in these simulations which allow the observation of shear bands and compare the stress–strain behaviour on different meshes. Depending on your choice of parameters it may be useful to solve the previous task first. Which parameters is the simulation most sensitive to and why? What is the result when using only one element?



## Chapter 4

# Simulating Gas Storage in Salt Caverns

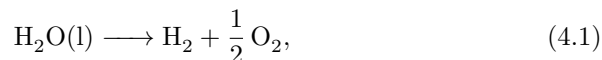
### 4.1 Scenario

Salt caverns are artificial cavities in salt formations, which are usually used for long-term storage of hydrocarbons such as black oil or natural gas. At least two facilities, located in MacIntosh, USA ([PowerSouth Energy Cooperative](#)) and in Huntorf, Germany ([Crotogino and Quast, 1981](#)), employ salt caverns in combination with compressed air energy storage (CAES).

Recently, salt caverns are being considered as promising storage sites for power-to-gas-to-power (P2G2P) applications within the context of renewable energy storage. In addition to compressed air, artificial methane or hydrogen could be utilised as working gases.

Compared to traditional gas tanks located on the surface, underground caverns have various advantages: the capacity (in terms of volume) of salt caverns is much higher; the volume of salt caverns can easily exceed gas tank volumes by factors of 100 to 1000. Furthermore, working pressures in caverns can be about ten times higher than gas tank pressures<sup>22</sup>. Artificial salt caverns are usually constructed by solution mining, a time-consuming but relatively cheap process.

Cavern operation is characterised by pressure changes. Depending on the cavern purpose, those pressure fluctuations can occur on a seasonal, weekly or even daily basis. In this example, we consider a comparatively small cavern used for short-term storage of hydrogen. Hydrogen is produced from fresh water utilising electrolyzers. These devices use electrical energy to decompose water molecules into oxygen and hydrogen in an endothermic reaction:



---

<sup>22</sup> The exception being small-scale CAES using high-pressure cylinders made of expensive carbon-fibre composites holding up to 300 bars, where the cycle number is limited by mechanical fatigue to a few tens of thousands ([Ibrahim et al., 2008](#)).

In other words, hydrogen represents a possible energy storage medium to store excess electricity by converting electrical energy into a chemical potential (P2G). The process of electrolysis can be reversed in a fuel cell thus closing the storage cycle (P2G2P). Theoretically, this exothermic oxidation releases the same amount of energy as it took for the electrolyzer to decompose the water molecules. In practice, both reactions suffer power losses, which can be quantified by an efficiency factor  $\eta$ . The required power for charging the cavern or the power released by discharging the cavern can be determined by

$$P = \eta \dot{m} \Delta H_{\text{R}}^{\circ} / M_{\text{H}_2} \quad (4.2)$$

provided that the efficiencies are known. In (4.2),  $\dot{m}$  is the mass flux during charging or discharging stages,  $M_{\text{H}_2}$  is the molar mass of hydrogen and  $\Delta H_{\text{R}}^{\circ} = 285.9 \text{ kJ mol}^{-1}$  is the reaction enthalpy of (4.1) for molecular hydrogen.

The following example covers a scenario, where a small hydrogen cavern is used as part of an emergency energy storage of a factory or a small town. In this scenario, the task is to bridge an unexpected energy gap in the network that lasts for several days. Our cavern is preloaded with its maximum operation pressure of  $p_{\text{max}} = 15 \text{ MPa}$ . When the power breakdown occurs, the stored hydrogen is discharged at a constant mass flux of  $\dot{m}_{\text{out}} = 0.1 \text{ kg s}^{-1}$ . Assuming a combined efficiency of the entire discharging process (all energy losses from friction, heat loss or fuel cell efficiencies combined) of  $\eta_{\text{out}} = 0.56$ , this mass flux corresponds to a power of about  $P_{\text{out}} = 7.9 \text{ MW}$ .

After five days, the cavern pressure has dropped below a predetermined threshold value  $p_{\text{min}} = 8.5 \text{ MPa}$ , thus the discharging process is stopped. However, the gap in the energy network remains and has to be bridged by other means, thus the cavern cannot be recharged.

Another five days later, surplus energy is available again and the refilling process of the cavern can be started. Here, the charging speed is limited by the hydrogen production rate. In our case, the cavern operator uses three electrolyzers with an individual production rate of  $\dot{V} = 670 \text{ m}^3 \text{ h}^{-1}$  at standard conditions. The maximum mass flux for this set-up is  $\dot{m} = 0.05 \text{ kg s}^{-1}$ , thus it requires 10 d to restore the initial cavern pressure.

Here, we use OpenGeoSys to investigate the effect of this scenario on the host rock of the cavern. For that purpose, we will cover two different approaches. At first, an isothermal example (4.3) will only consider the effects of the pressure drop in the cavern. The pressure change has no influence on the gas temperature and is thus only governed by the mass flux. In the second example (4.4), the thermodynamic effects accompanying the gas pressure changes are considered. A thermo-mechanical analysis will be performed to study how the resulting temperature variation influences the material properties of and the stress fields in the host rock.

## 4.2 General set-up

In this section, the general definitions of the model set-up for both examples are described. The reader may find additional information on the various input files in the previous chapter, pages 23ff.

### *Cavern geometry*

With a volume of about  $10\,000\text{ m}^3$ , the salt cavern in this example is relatively small. Its geometry is idealised and can be described as a cylinder with hemispherical ends. The cavern has a radius of 6 m and a length of 92 m, as measured at the centre line.

The model domain of this example represents the surrounding host rock of our salt cavern. Basically, this domain is represented by a cylinder with a radius of 250 m, a height of 294 m containing the cavity in its centre. The top of the domain is located at a depth of  $-1000\text{ m}$  below the surface.

To spatially discretise this set-up for numerical analysis, we make use of the advantage that the geometry of both cavern and domain cylinder is rotationally symmetric around a central axis. Therefore, the entire model domain can be reduced to a planar representation consisting of only a few thousand elements, described in cylindrical coordinates, see Fig. 4.1. This approach is commonly used, but it is limited to analyses of single caverns in formations which are circumferentially homogeneous around the axis of symmetry. In contrast, considering the interactions of multiple caverns in cavern fields requires a three-dimensional discretisation. The size, shape, location, and connectivity of those elements is defined in the MSH-file. For this example, the corresponding mesh file and all other input files are available on the *OGS website* <https://docs.opengeosys.org/books>. For more info on meshing, see the introductory section of Chapter 3 on page 23.

In order to apply boundary conditions and to define locations for result output, the GLI-file defines geometrical entities such as points, polylines, or surfaces. Listing 4.1 shows an example of how points and polylines are defined. In our example, we define three polylines TOP, BOT, and RIGHT to represent the outer surface of the model domain, two polylines TOP\_LEFT and BOT\_LEFT for the symmetry axis, and one polyline CAVERN for the cavern wall. The points B to F are defined for output reasons only. The location of these geometrical objects as well as a schematic of the entire domain is illustrated in Fig. 4.1.

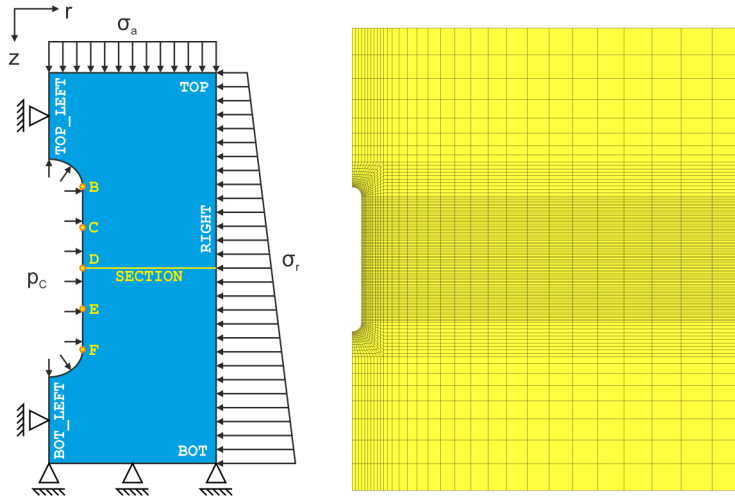


Fig. 4.1: Schematic view with boundary conditions (left) as well as the spatial discretisation (right) of the cavern model.

Listing 4.1: Cavern geometry.

```
#POINTS
0 0.000e+00 -1.000e+06 0.000e+00 $NAME P_0
...
122 0.000e+00 -1.294e+06 0.000e+00 $NAME P_122
123 2.500e+05 -1.294e+06 0.000e+00 $NAME P_123
124 2.500e+05 -1.147e+06 0.000e+00 $NAME P_124
125 2.500e+05 -1.000e+06 0.000e+00 $NAME P_125
...
#POLYLINE
$NAME
TOP
$POINTS
0
125
...
```

### *Initial conditions*

As mentioned before, the history of the stress state is not taken into account in this example. A hydrostatic stress distribution is assumed to characterize the initial state of the cavern. This condition can be applied via initial conditions. Here, however, it will be generated directly during the first time steps.

Therefore, the initial state is given by zero-stress and zero-strain conditions, which do not need to be defined explicitly in the IC-file.

### *Boundary conditions*

In the BC-file, Dirichlet boundary conditions are specified. For the deformation process, Dirichlet boundary conditions define the displacements imposed on the model domain.

Since our model domain is described as axisymmetric, displacements at the symmetry axis are allowed in axial (vertical) direction only. The example domain is joined to this axis by two polylines, `TOP_LEFT` and `BOT_LEFT` (Fig. 4.1) which are separated by the cavern. Thus, for each of these polylines, an individual boundary condition has to be specified. At the bottom of the domain, represented by the polyline `BOT`, displacements in the vertical direction are suppressed.

To assign a Dirichlet boundary condition, the following keywords are required: `#BOUNDARY_CONDITION` initializes a new block where the Dirichlet-condition is specified. `$PCS_TYPE` refers to the name of the process for which the boundary condition is required. `$PRIMARY_VARIABLE` specifies which of the primary variables of a process is to be assigned a boundary value. The location, at which the boundary value is applied is specified by the `$GEO_TYPE`-keyword. This may refer to `POINT(s)`, `POLYLINE(s)`, or `SURFACE(s)`. The `$DIS_TYPE`-keyword refers to how the boundary value is distributed spatially over the specified subdomain. The most common distribution types are `CONSTANT` and `LINEAR`. In this example, the Dirichlet boundary conditions are constant over both time and location. Thus, as shown in Listing 4.2, the distribution type `CONSTANT` was chosen, followed by the actual Dirichlet value (0.0 in this case).

Listing 4.2: Three displacement constraints for an axisymmetric cavern problem.

```
#BOUNDARY_CONDITION
$PCS_TYPE
  DEFORMATION
$PRIMARY_VARIABLE
DISPLACEMENT_X1
$GEO_TYPE
  POLYLINE TOP_LEFT
$DIS_TYPE
CONSTANT 0.0

#BOUNDARY_CONDITION
$PCS_TYPE
  DEFORMATION
$PRIMARY_VARIABLE
DISPLACEMENT_X1
$GEO_TYPE
  POLYLINE BOT_LEFT
$DIS_TYPE
CONSTANT 0.0

#BOUNDARY_CONDITION
$PCS_TYPE
  DEFORMATION
$PRIMARY_VARIABLE
DISPLACEMENT_Y1
$GEO_TYPE
  POLYLINE BOT
$DIS_TYPE
CONSTANT 0.0
```

Note that although this example is described and computed in cylinder coordinates, the names of the keywords does not deviate from Cartesian problems. Thus, `DISPLACEMENT_X1` refers to radial, while `DISPLACEMENT_Y1` refers to the axial direction in this 2D example corresponding to the mesh file.

### *Source terms*

The `ST`-file defines boundary conditions of the Neumann type. For the deformation process, it allows to apply tractions at specific geometrical entities.

In our example, a constant stress in the vertical direction is applied to the top of the domain acting as an overburden pressure. The top of the model domain is located at a depth of  $z = -1000$  m in a rock salt dome with a density of  $\rho_{\text{salt}} = 2040 \text{ kg m}^{-3}$ . This salt formation is covered by solid rock with an average density of  $\rho_{\text{rock}} = 2500 \text{ kg m}^{-3}$ . The interface between rock salt and solid rock is located at  $z = -800$  m, thus the overburden stress can be found to be about  $\sigma_a = -23.62 \text{ MPa}$ .

Similarly to the Dirichlet-boundary conditions in the `BC`-file, the Neumann-conditions are assigned by a code-block initialised by the keyword

`#SOURCE_TERM`. Within this code-block, the keywords `$PCS_TYPE`, `$PRIMARY_VARIABLES`, and `$GEO_TYPE` can be used in the same way as described in the previous section. For the distribution type, a new option `CONSTANT_NEUMANN` distributes the boundary value evenly over the specified geometry in the sense of a traction distribution. The following listing shows the assignment for the overburden stress.

Listing 4.3: Constant overburden loading at the top of the domain.

```
#SOURCE_TERM
$PCS_TYPE
  DEFORMATION
$PRIMARY_VARIABLE
  DISPLACEMENT_Y1
$GEO_TYPE
  POLYLINE TOP
$DIS_TYPE
  CONSTANT_NEUMANN -2.362248e+01
$TIM_TYPE
  CURVE 1
```

Note here that the specified value of  $\sigma_a = -23.62$  MPa is constant over the polyline `TOP`, but the temporal distribution is specified by a scaling function. The use of such a scaling function is enabled by the keyword `$TIM_TYPE`. All such functions are defined in the `RFD`-file (see below), and specific scaling functions are referred by a successive number (order of appearance in the `RFD`-file). Thus, `CURVE 1` refers here to the first scaling function defined in the `RFD`-file. The resulting Neumann-value assigned to the specified geometry is simply the product of the value given by `$DIST_TYPE` and the value of the scaling function at a certain time. In our example, a scaling function is used as a ramp for all Neumann-type boundary conditions in order to apply their values gradually over time during the first time steps. This measure is taken in order to ensure a faster convergence of the numerical solver.

To achieve a hydrostatic stress state, a linear load following the lithostatic pressure gradient is applied to the right boundary of the domain (Fig. 4.1). This linear distribution is obtained by introducing the distribution type `LIN-EAR_NEUMANN`, as shown in the following example, Listing 4.4:

Listing 4.4: Linearly increasing lithostatic pressure at the right boundary of the domain.

```
#SOURCE_TERM
$PCS_TYPE
  DEFORMATION
$PRIMARY_VARIABLE
DISPLACEMENT_X1
$GEO_TYPE
  POLYLINE RIGHT
$DIS_TYPE
  LINEAR_NEUMANN 2
    125 -2.362248e+01
    123 -2.9506126e+01
$TIM_TYPE
CURVE 1
```

The number following the distribution-type option refers to the number of supporting points of the desired boundary value distribution. From the next line on, OpenGeoSys expects a list of points and corresponding values. Those points are specified using the point-ID as given in the `GLI`-file, (first column of the `#POINTS` list, see Listing 4.1). The number of rows of that list must be equal to the number of supporting points as specified after the `LINEAR_NEUMANN`-statement. It is possible to assign multiple sections with different slopes of the distribution function by including more than two points in this list.

In this example, we only need two points specifying the start and end values of our lithostatic stress. Node number 125 refers to the top right, while node number 123 refers to the bottom right corner of the domain. For all nodes located on polyline `RIGHT`, a value is assigned that was interpolated linearly between the specified start and end values.

To keep this example simple, the construction stage of the cavern is not considered, and the initial pressure in the cavern corresponds to the maximum loading pressure  $p_{\max} = 15$  MPa. The definition of the cavern pressure is applied to the polyline `CAVERN`, as shown in Listing 4.5. In contrast to the polylines `TOP` or `RIGHT`, some parts of that polyline are not parallel to any coordinate axis. Thus, the new subkeyword `DISPLACEMENT_N` is used, which refers to a traction boundary condition that acts perpendicular to the specified geometry ("pressure boundary condition").

Listing 4.5: Assigning the cavern pressure.

```

#SOURCE_TERM
$PCS_TYPE
DEFORMATION
$PRIMARY_VARIABLE
DISPLACEMENT_N
$GEO_TYPE
POLYLINE CAVERN
$DIS_TYPE
CONSTANT_NEUMANN -1.0
$TIM_TYPE
CURVE 2

```

In order to obtain more realistic results, the excavation process of the cavern construction could be taken into account. Methods to consider this cavern excavation for OpenGeoSys-simulations are described in [Böttcher et al. \(2017\)](#); [Görke et al. \(2012\)](#).

### *Time discretisation*

The definition of the temporal discretisation is specified in the TIM-file. A keyword `#TIME_STEPPING` opens a new block containing all specifications defining the time-stepping scheme of a process.

If multiple processes are coupled, an individual time-stepping scheme can be defined for each process by the `$PCS_TYPE`-subkeyword. We use fixed time steps in this example, where the time-step length is linked to the defined mass flux in the cavern. In [Fig. 4.2](#), two different time-stepping schemes are plotted in conjunction with the mass flux of the working gas. Both schemes have in common that whenever the mass flux changes, time-step sizes are reduced. Scheme A is a simpler approach, while scheme B is more adapted to the boundary conditions and thus consists of even more time steps defined in the time stepping file.

The parameters of scheme A are given in [Listing 4.6](#).



### 4.3 Isothermal model set-up

In this part of the example, we consider only the effects of cavern pressure drop and ignore the temperature variations due to expanding gases. When temperature is constant, the cavern pressure is determined by gas mass only. At atmospheric levels, the ideal gas law is sufficient to obtain the pressure of a gas. However, since the pressures in cavern operations are one to two orders of magnitude higher, this idealised concept cannot be applied. Therefore, we use the equation of state for real gases proposed by Peng and Robinson

$$p = \frac{RT}{v_m - b} - \frac{a}{v_m^2 + 2bv_m - b^2} \quad (4.3)$$

where  $v_m$  is the molar volume of the gas,  $R$  is the universal gas constant, and  $a$  and  $b$  are substance-specific parameters. For the definition of  $a$  and  $b$ , we refer to the original publication (Peng and Robinson, 1976). Since the mass flux is known in our example, molar volume as function of time can be found by

$$v_m(t) = \frac{V_{\text{cav}} M_{\text{H}_2}}{m(t)} \quad (4.4)$$

with cavern volume  $V_{\text{cav}}$  and molar mass of hydrogen  $M_{\text{H}_2}$ . From (4.3) and (4.4), the pressure evolution inside the cavern can be determined for the isothermal case (see Fig. 4.3). This pressure function, written as a time series, serves as the scaling function for our previously defined Neumann-Boundary condition for the cavern pressure. In Listing 4.5, we referred to the second curve in the RFD-file for this purpose. The concept of this scaling function definition in the RFD-file is fairly simple: A new scaling function is initialised by the `#CURVE`-keyword, followed by a table with two columns. The first of these columns contains a time point, the second one contains the corresponding value of the scaling function. Values between given points in time are interpolated linearly. Listing 4.7 exemplarily illustrates the scaling function for the cavern pressure.

Listing 4.7: Example for a scaling function in the RFD-file.

```

; curve 2
#CURVES
0.00 0.0000000
1.00 15.0000000
9.90 15.0000000
10.00 14.8256211
...
15.00 8.1791913
15.10 8.2147679
15.20 8.2485267
...
20.00 8.9195730
20.10 9.0151044
20.20 9.1088953
...
30.00 16.0063734
30.10 15.9748615
30.20 15.9443362
...
99.80 15.0000000
99.90 15.0000000
100.0 15.0000000
10000 15.000000

```

### *Material properties*

To describe rock-salt behaviour, the LUBBY2 material model described in Section 2.5 by Eqs. (2.44)–(2.51). The same parameters as given in Table 3.2 are used, see Listing 4.8 as well as Listing 3.7.

Listing 4.8: Solid properties for the isothermal cavern simulation.

```

#SOLID_PROPERTIES
$DENSITY
1 2.04e-06
$CREEP_BURGERS
;G_KO, m_K, eta_KO, mv_K G_MO, K_MO, eta_MO, \
mvM m_GM m_KM T_ref B Q
6.2667e4 -2.54e-1 1.66e5 -2.67e-1 9.5420E+003 2.7798E+004 4.03e7 \
-3.27e-1 0.0 0.0 313 1.0 0.0
$GRAVITY_RAMP
1 9.81

```

In contrast to the laboratory test examples from Section 3, the size of the cavern model is so large that the gravity field has a significant influence on the stress state throughout the domain. In order to apply this gravity load gradually over the first time steps, the keyword \$GRAVITY\_RAMP is used. The succeeding specifications define the scaling function in the RFD-File (1), as well as the magnitude of gravitational acceleration ( $9.81 \text{ m s}^{-2}$ ).

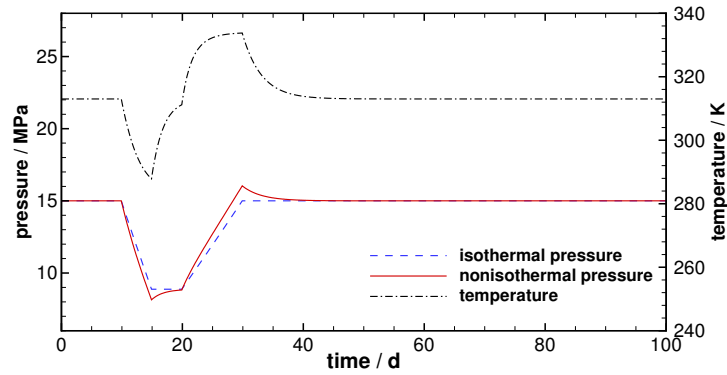


Fig. 4.3: Cavern pressures when temperature (black, dash-dotted) is either ignored (blue, dashed) or considered (red, solid).

#### 4.4 Non-isothermal model set-up

For the non-isothermal simulation, a heat transport process needs to be added to the simulation. Refer to Listing 3.1 in Section 3.1 on page 24 regarding the necessary set-up.

##### *Initial conditions*

The initial temperature was derived from the geothermal gradient. In the considered depth of  $z = -1100$  m, the temperature is assumed to be  $T = 313$  K. The thermal gradient within the model domain is ignored, thus the initial temperature is evenly distributed over the entire domain for the sake of simplicity.

Listing 4.9: Assigning the initial temperature in the domain.

```
#INITIAL_CONDITION
$PCS_TYPE
HEAT_TRANSPORT
$PRIMARY_VARIABLE
TEMPERATURE1
$GEO_TYPE
DOMAIN
$DIS_TYPE
CONSTANT 313
```

## *Boundary conditions*

For the non-isothermal example, the boundary condition specification is extended by the Dirichlet boundary condition for the heat transport process. Since the gas temperature is changing, it is specified by a scaling function `CURVE 3`, defined in the `RFD`-file. In this case, the scaling function consists of the actual temperature values, which are multiplied by the value defined in the `BC`-file, (see Listing 4.10). The temperature time series was obtained using a simplified analytical method proposed by Xia et al. (2015), which assumes that the gas density at a given time step is constant and that heat conduction process in the rock salt occurs very fast. The resulting temperature curve is plotted over time in Fig. 4.3. One can notice that the temperature drops from 313 K to 288 K during discharge. During the idling period, the temperature recovers almost to its initial value due to the heat backflow from the rock salt. When the cavern is recharged, the temperature rises due to gas compression to almost 334 K. After the recharge stage is completed, the temperature equalises to initial conditions within several days. Using this temperature curve, the corresponding gas pressure was calculated using (4.3). In the same way as in the isothermal case, it is defined as scaling function `CURVE 2` in the `RFD`-file.

Listing 4.10: Temperature boundary condition for the non-isothermal cavern example.

```
#BOUNDARY_CONDITION
$PCS_TYPE
HEAT_TRANSPORT
$PRIMARY_VARIABLE
  TEMPERATURE1
$GEO_TYPE
  POLYLINE CAVERN
$DIS_TYPE
  CONSTANT 1
$TIM_TYPE
  CURVE 3
```

## *Material properties*

The `MSP`-file changes compared to Listing 4.8 by adding parameters for the temperature dependence as well as the heat transport process; compare also Listing 3.7.

Listing 4.11: Temperature-dependent material parameters.

```

$CREEP_BURGERS
;G_K0,      m_K,      eta_K0,  mv_K      G_MO,      K_MO,      eta_MO,  \
mvM        m_GM      m_KM      T_ref     B          Q
6.2667e4   -2.54e-1  1.66e5   -2.67e-1  9.5420E+03 2.7798E+04 4.0333e7
\
-3.27e-1  -21.1405  -25.265  313  1.0  16000
$THERMAL
EXPANSION 2.8e-05
CAPACITY
1 920
CONDUCTIVITY
1 648
$GRAVITY_RAMP
1 9.81

```

For other settings regarding the coupled process, such as solvers, time stepping etc., please refer to Section 3.1.

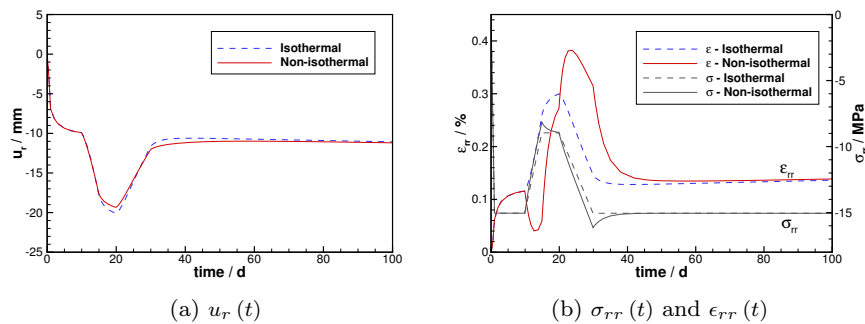


Fig. 4.4: Radial displacement as well as radial components of stress and strain tensors versus time, plotted at the centre of the cavern wall (point D).

## 4.5 Comparison of results

To visualise the simulation results, we consider the entire domain, a profile at the level of the cavern centre (polyline `SECTION`), and a single point at the cavern wall at the same elevation (point D), cf. Fig. 4.1.

The radial displacement of the cavern wall is shown in Fig. 4.4a. At the very beginning of the simulation, this displacement grows rapidly and is directed towards the cavern centre. Within the first day, this displacement results primarily from elastic deformations. For the remaining nine days prior to

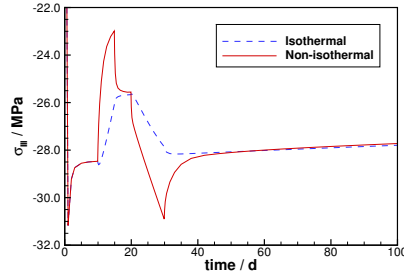


Fig. 4.5: Third principal stress over time at point D.

the pressure drop, the deformation rate decreases but does not yet reach the steady-state (secondary) creep phase.

This behaviour is caused by the simplified initial conditions of the examples. This issue can be circumvented in two ways: either by the assignment of initial stress and internal variable fields using initial conditions, or by a shift of the beginning of the simulation towards earlier times such that the entire history of the cavern (including the solution mining or excavation process) or a relevant part of it are included in the simulation (Böttcher et al., 2017). Finding a suitable initial stress and material state may require simulating part of the history, which is why the latter option is often preferred. The former option, however, should be applied when obtaining these results by history simulations is very time consuming and a stored initial state renders a re-calculation unnecessary. This requires consistent data fields of stresses, strains, necessary internal variables and temperatures over the entire simulation domain.

With the beginning discharging stage, the radial displacement towards the centre line is growing due to the pressure drop in the cavern. The resulting displacements are similar in both isothermal and non-isothermal examples, but the displacement amplitude between discharged and recharged stages is larger in case of the isothermal simulation, although the pressure amplitude of the boundary condition is slightly smaller when temperature variations are ignored (compare Fig. 4.3).

The reason for this behaviour is the thermal contraction or expansion of the material in the non-isothermal case. When working gas is discharged, temperature drops and the rock salt contracts. Considering the radial strain, Fig. 4.4b shows the effect of material contraction more clearly. From  $t = 10$  d, the radial strain rate is negative in the non-isothermal case due to contraction. Similarly, during gas injection, the temperature rise leads to thermal expansion in the heated region, thereby increasing the radial strain. Taken together, both mechanisms explain the apparent “phase-shift” between the strain curves in the isothermal and non-isothermal cases in Fig. 4.4b.

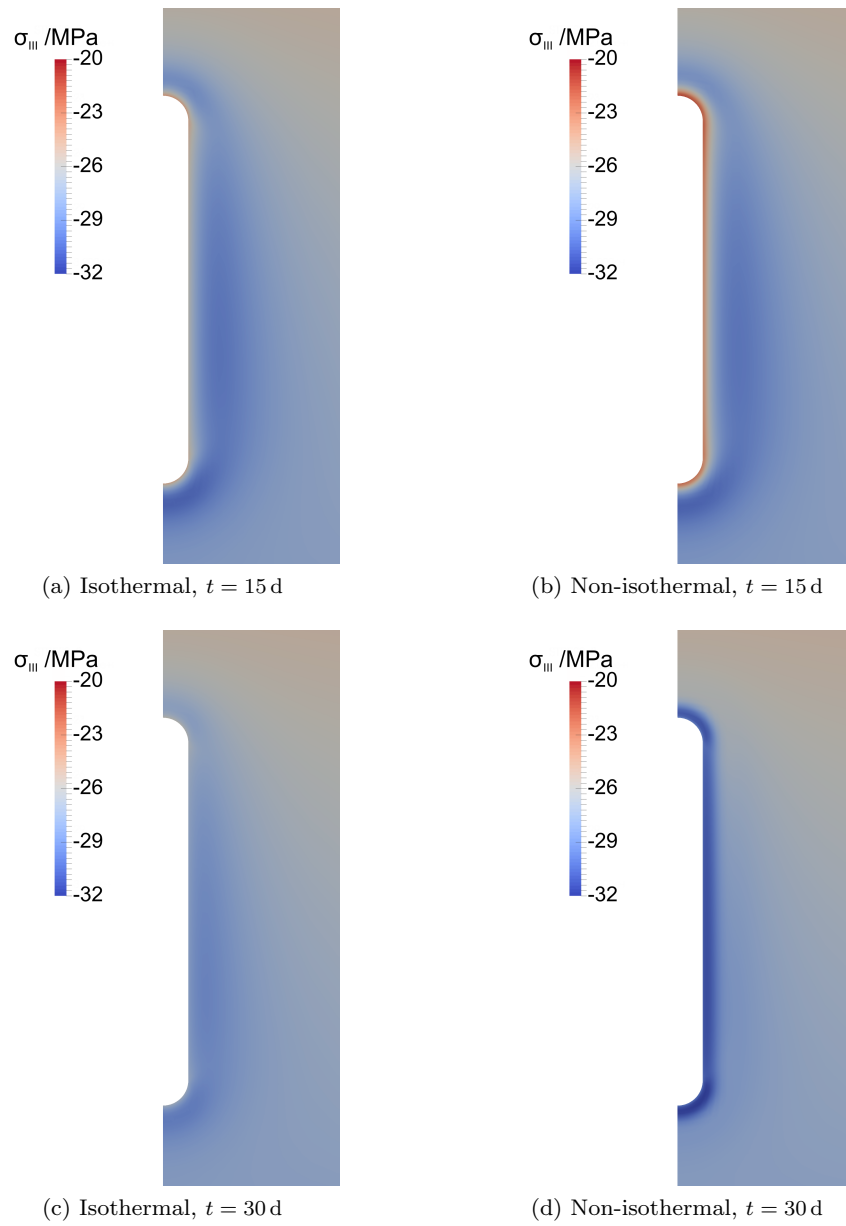


Fig. 4.6: Third principal stress around the cavern for the isothermal case (a, c) and the non-isothermal case (b, d).

Contraction and expansion furthermore influence the stress fields; in Fig. 4.5, the third principal stress amplitude is shown to grow when con-

sidering thermal effects; this effect of more higher and lower stress peaks is also visible in Fig. 4.6, which compares the distribution of the third principal stress in the vicinity of the cavern at discharged and recharged stages for both scenarios. The direct influence of temperature can be observed when comparing Fig. 4.7 to Fig. 4.8. When the principal stresses are plotted along the cross-section of the domain at the cavern centre (polyline SECTION, see Fig. 4.1), one can observe that the effect is restricted to the vicinity of the cavern wall (up to about  $r = 5$  m); with increasing distance from the wall, differences between isothermal and non-isothermal examples are decreasing (Fig. 4.7).

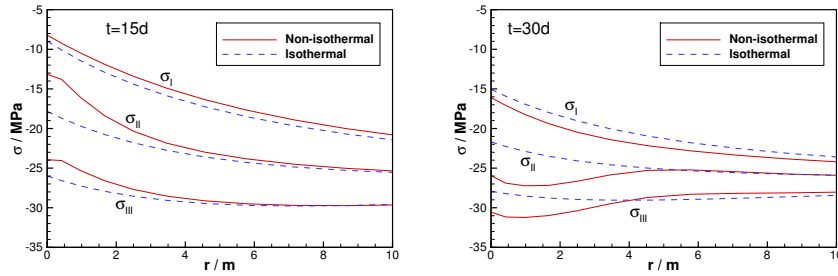
(a) Principal stress profile at  $t = 15$  d.(b) Principal stress profile at  $t = 30$  d.

Fig. 4.7: The profiles of principal stresses in the vicinity of the cavern wall when the cavern is fully discharged ( $t = 15$  d, a) and when its fully recharged ( $t = 30$  d, b).

Likewise, Fig. 4.8 shows comparable trends for the temperature profile. Large temperature amplitudes can be found only adjacent to the cavern wall. From  $r = 6.25$  m, the temperature amplitudes drop below  $\Delta T = 1$  K.

For a first evaluation of structural safety, one can apply a Mohr-Coulomb failure criterion. Structural failure will occur when shear stresses exceed a predefined failure envelope. The shear strength of the material grows linearly with mean stress  $\sigma_m = 1/3 \text{tr } \boldsymbol{\sigma}$  and is defined as

$$\tau_m = c - \sigma_m \tan \phi \quad (4.5)$$

where  $c$  and  $\phi$  are the cohesion and the angle of inner friction, respectively. For the defined material model,  $c$  and  $\phi$  are constants given by  $c = 8.218$  and  $\phi = 44.654^\circ$ . The maximal shear stress at a point can be found by

$$\tau_{\max} = \frac{1}{2} (\sigma_I - \sigma_{III}). \quad (4.6)$$

The failure ratio

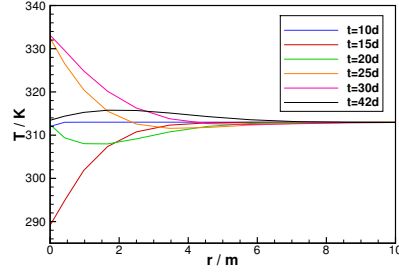


Fig. 4.8: Temperature profile at different points in time in the vicinity of the cavern wall.

$$\text{FR} = \frac{\tau_{\max}}{\tau_m} \quad (4.7)$$

is an inverse safety factor and indicates the material condition in terms of the distance to structural failure. Small values of FR represent safe conditions below the failure envelope. At  $\text{FR} = 1$ , structural failure occurs. In Fig. 4.9, the failure ratio is plotted over the hydrostatic pressure  $p = -\sigma_m$  for point D at the centre of the cavern wall. In both isothermal and non-isothermal examples, the failure ratio is similar, remaining safely below  $\text{FR} = 0.4$ , so structural failure does not occur according to this criterion.

A more detailed study of this and other relevant safety criteria accompanied with cyclic cavern loading patterns can be found in (Böttcher et al., 2017).

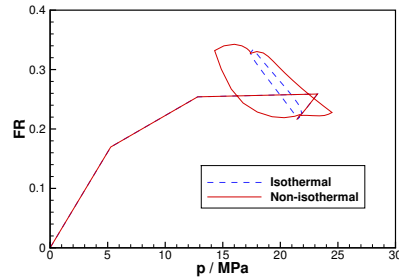


Fig. 4.9: Failure ratio as quotient of shear strength  $\tau_m$  and maximum shear stress  $\tau_{\max}$  for both isothermal and non-isothermal examples, plotted at the centre of the cavern wall.



## Chapter 5

### Closing remarks

This book gave an introduction into the thermo-mechanical modelling of rock salt in general, and of gas storage in salt caverns in particular. There are many topics that were not discussed here but that are very relevant: fracturing, fluid percolation, the influence of realistic three-dimensional geometries, safe cavern abandonment, etc. For now, we refer the reader to the wealth of literature cited here and referenced in those citations.

OpenGeoSys is constantly growing with new material models, processes, and features becoming available. We would like to encourage a regular visit to [www.opengeosys.org](http://www.opengeosys.org). There, you can also find examples on how to include a coupling to fluid flow in the simulations, which we did not address here.

Last but not least, any active participation is greatly appreciated. If you would like to extend the software, implement other, better models, don't hesitate to download the source code, extend it, and send us a pull-request via GitHub. How to do that? Find out at—you guessed it—<https://docs.opengeosys.org/docs>.



## References

- Adamson, K.-A., 2004. Hydrogen from renewable resources—the hundred year commitment. *Energy Policy* 32 (10), 1231–1242.
- Bathe, K., 2014. *Finite Element Procedures*, 2nd Edition. Klaus-Jürgen Bathe.
- Bauer, S., Beyer, C., Dethlefsen, F., Dietrich, P., Duttmann, R., Ebert, M., Feeser, V., Görke, U., Köber, R., Kolditz, O., Rabbel, W., Schanz, T., Schäfer, D., Würdemann, H., Dahmke, A., 2013. Impacts of the use of the geological subsurface for energy storage: an investigation concept. *Environmental Earth Sciences* 70 (8), 3935–3943.
- Böttcher, N., Görke, U.-J., Kolditz, O., Nagel, T., 2017. Thermo-mechanical investigation of salt caverns for short-term hydrogen storage. *Environmental Earth Sciences* 76 (3), 98.
- Böttcher, N., Watanabe, N., Görke, U.-J., Kolditz, O., 2016. *Geoenergy Modeling I*. Springer-Verlag GmbH.
- Cacace, M., Blöcher, G., 2015. MeshIt—a software for three dimensional volumetric meshing of complex faulted reservoirs. *Environmental Earth Sciences* 74 (6), 5191–5209.
- Chan, K., Brodsky, N., Fossum, A., Bodner, S., Munson, D., 1994. Damage-induced nonassociated inelastic flow in rock salt. *International Journal of Plasticity* 10 (6), 623–642.
- Cristescu, N., 1985. Irreversible dilatancy or compressibility of viscoplastic rock-like materials and some applications. *International Journal of Plasticity* 1 (3), 189–204.
- Cristescu, N., 1994. A procedure to determine nonassociated constitutive equations for geomaterials. *International Journal of Plasticity* 10 (2), 103–131.
- Cristescu, N. D., Hunsche, U., 1998. *Time effects in rock mechanics*. Wiley New York.
- Crotogino, F., Donadei, S., Bünger, U., Landinger, H., 2010. Large-scale hydrogen underground storage for securing future energy supplies. In: 18th World hydrogen energy conference. Vol. 78. pp. 37–45.

- Crotogino, F., Quast, P., 1981. Compressed-Air Storage Caverns at Huntorf. In: Bergman, M. (Ed.), *Subsurface Space*. Pergamon, pp. 593 – 600.
- de Borst, R., Heeres, O. M., 2002. A unified approach to the implicit integration of standard, non-standard and viscous plasticity models. *International Journal for Numerical and Analytical Methods in Geomechanics* 26 (11), 1059–1070.
- Desai, C., Zhang, D., 1987. Viscoplastic model for geologic materials with generalized flow rule. *International Journal for Numerical and Analytical Methods in Geomechanics* 11 (6), 603–620.
- Du, C., Yang, C., Yao, Y., Li, Z., Chen, J., 2012. Mechanical Behaviour of Deep Rock Salt under the Operational Conditions of Gas Storage. *International Journal of Earth Sciences and Engineering* 5 (6), 1670–1676.
- Forest, S., Lorentz, E., et al., 2004. Localization phenomena and regularization methods. *Local approach to fracture*, 311–371.
- Gahleitner, G., 2013. Hydrogen from renewable electricity: An international review of power-to-gas pilot plants for stationary applications. *International Journal of Hydrogen Energy* 38 (5), 2039–2061.
- Görke, U.-J., Günther, H., Nagel, T., Wimmer, M., 2010. A Large Strain Material Model for Soft Tissues With Functionally Graded Properties. *J Biomech Eng* 132 (7), 074502.
- Görke, U.-J., Kaiser, S., Bucher, A., Kreißig, R., 2012. A consistent mixed finite element formulation for hydro-mechanical processes in saturated porous media at large strains based on a generalized material description. *European Journal of Mechanics A/Solids* 32, 88–102.
- Görke, U.-J., Watanabe, N., Taron, J., Wang, W., 2012. Deformation Processes. In: Kolditz, O. and Görke, U.-J. and Shao, H. and Wang, W., *Thermo-hydro-mechanical-chemical processes in fractured porous media*, *Lecture Notes in Computational Science and Engineering* 86 LNCSE, 89–106.
- Greenblatt, J. B., Succar, S., Denkenberger, D. C., Williams, R. H., Socolow, R. H., 2007. Baseload wind energy: modeling the competition between gas turbines and compressed air energy storage for supplemental generation. *Energy Policy* 35 (3), 1474–1492.
- Hampel, A., Günther, R., Salzer, K., Minkley, W., Pudewills, A., Leuger, B., Zapf, D., Rokahr, R., Herchen, K., Wolters, R., et al., 2010. BMBF-Verbundprojekt: Vergleich aktueller Stoffgesetze und Vorgehensweisen anhand von 3D-Modellberechnungen zum mechanischen Langzeitverhalten eines realen Untertagebauwerks im Steinsalz. Tech. rep.
- Harris, A. F., McDermott, C., Kolditz, O., Haszeldine, R., 2015. Modelling groundwater flow changes due to thermal effects of radioactive waste disposal at a hypothetical repository site near Sellafield, UK. *Environmental Earth Sciences* 74 (2), 1589–1602.
- Haupt, P., 2002. *Continuum mechanics and theory of materials*. Springer.

- Heeres, O. M., Suiker, A. S., de Borst, R., 2002. A comparison between the Perzyna viscoplastic model and the consistency viscoplastic model. *European Journal of Mechanics-A/Solids* 21 (1), 1–12.
- Heusermann, S., Lux, K.-H., Rokahr, R., 1983. Entwicklung mathematisch-mechanischer Modelle zur Beschreibung des Stoffverhaltens von Salzgestein in Abhängigkeit von der Zeit und der Temperatur auf der Grundlage von Laborversuchen mit begleitenden kontinuumsmechanischen Berechnungen nach der Methode der finiten Elemente. Fachinformationszentrum Energie, Physik, Mathematik Karlsruhe.
- Heusermann, S., Rolfs, O., Schmidt, U., 2003. Nonlinear finite-element analysis of solution mined storage caverns in rock salt using the LUBBY2 constitutive model. *Computers & Structures* 81 (8–11), 629 – 638, k.J Bathe 60th Anniversary Issue.
- Holzapfel, G. A., 2000. *Nonlinear Solid Mechanics: A Continuum Approach for Engineering*. John Wiley & Sons Ltd.
- Hunsche, U., Schulze, O., 1994. Das Kriechverhalten von Steinsalz. *Kali und Steinsalz* 11 (8/9), 238–255.
- Hutter, K., Jöhnk, K., 2004. *Continuum methods of physical modeling: continuum mechanics, dimensional analysis, turbulence*. Springer.
- Ibrahim, H., Ilinca, A., Perron, J., 2008. Energy storage systems – characteristics and comparisons. *Renewable and Sustainable Energy Reviews* 12 (5), 1221–1250.
- Itskov, M., 2009. *Tensor algebra and tensor analysis for engineers: With applications to continuum mechanics*, 2nd Edition. Springer, Dordrecht.
- Jeremic, B., 2001. Line search techniques for elasto-plastic finite element computations in geomechanics. *Communications in numerical methods in engineering* 17 (2), 115–126.
- Jin, J., Cristescu, N., 1998. An elastic/viscoplastic model for transient creep of rock salt. *International Journal of Plasticity* 14 (1), 85–107.
- Kabuth, A., Dahmke, A., Beyer, C., Bilke, L., Dethlefsen, F., Dietrich, P., Duttmann, R., Ebert, M., Feeser, V., Görke, U.-J., Köber, R., Rabbel, W., Schanz, T., Schäfer, D., Würdemann, H., Bauer, S., 2016. Energy storage in the geological subsurface: dimensioning, risk analysis and spatial planning: the ANGUS+ project. *Environmental Earth Sciences* 76 (1), 23.
- Kolditz, O., Görke, U.-J., Shao, H., Wang, W. (Eds.), 2012. *Thermo-Hydro-Mechanical-Chemical Processes in Porous Media*. Lecture Notes in Computational Science and Engineering. Springer-Verlag GmbH.
- Kolditz, O., Görke, U.-J., Shao, H., Wang, W., Bauer, S. (Eds.), 2016. *Thermo-Hydro-Mechanical-Chemical Processes in Fractured Porous Media: Modelling and Benchmarking*. Benchmarking Initiatives. Terrestrial Environmental Sciences. Springer-Verlag GmbH.
- Kolditz, O., Shao, H., Wang, W., Bauer, S. (Eds.), 2014. *Thermo-Hydro-Mechanical-Chemical Processes in Fractured Porous Media: Modelling and Benchmarking*. Closed Form Solutions. Terrestrial Environmental Sciences. Springer International Publishing.

- Kolymbas, D., Fellin, W., Schneider-Muntau, B., Medicus, G., Schranz, F., 2016. Zur Rolle der Materialmodelle beim Standsicherheitsnachweis. *geotechnik* 39 (2), 89–97.
- Lewis, R. W., Schrefler, B. A., 1998. *The finite element method in the static and dynamic deformation and consolidation of porous media*, 2nd Edition. Wiley, Chichester [u.a.].
- Li, M., Zhang, H., Xing, W., Hou, Z., Were, P., 2015. Study of the relationship between surface subsidence and internal pressure in salt caverns. *Environmental Earth Sciences* 73 (11), 6899–6910.
- Lund, H., Salgi, G., 2009. The role of compressed air energy storage (CAES) in future sustainable energy systems. *Energy Conversion and Management* 50 (5), 1172–1179.
- Lund, H., Salgi, G., Elmegaard, B., Andersen, A. N., 2009. Optimal operation strategies of compressed air energy storage (CAES) on electricity spot markets with fluctuating prices. *Applied Thermal Engineering* 29 (5), 799–806.
- Lux, K.-H., 1984. *Gebirgsmechanischer Entwurf und Felderfahrungen im Salzkavernenbau: ein Beitrag zur Entwicklung von Prognosemodellen für den Hohlraumbau im duktilen Salzgebirge*. Ferdinand Enke Verlag, Stuttgart.
- Lux, K. H., Rokahr, R., 1984. Laboratory investigations and theoretical statements as a basis for the design of cavern in rock salt formation. In: *Proceedings of the 1st Conference on the Mechanical Behavior of Salt*. pp. 169–179.
- Ma, H., Yang, C., Li, Y., Shi, X., Liu, J., Wang, T., 2015. Stability evaluation of the underground gas storage in rock salts based on new partitions of the surrounding rock. *Environmental Earth Sciences* 73 (11), 6911–6925.
- Markert, B., 2013. A survey of selected coupled multifield problems in computational mechanics. *Journal of Coupled Systems and Multiscale Dynamics* 1 (1), 22–48.
- Mehrabadi, M. M., Cowin, S. C., 1990. Eigensensors of Linear Anisotropic Elastic Materials. *The Quarterly Journal of Mechanics and Applied Mathematics* 43 (1), 15–41.
- Minkley, W., 2004. *Gebirgsmechanische Beschreibung von Entfestigung und Sprödbrucherscheinungen im Carnallit*. Shaker.
- Minkley, W., Knauth, M., Brückner, D., 2013. Discontinuum-mechanical behaviour of salt rocks and the practical relevance for the integrity of salinar barriers. In: *47th US Rock Mechanics/Geomechanics Symposium*. American Rock Mechanics Association.
- Minkley, W., Knauth, M., Fabig, T., Farag, N., 2015. Stability and integrity of salt caverns under consideration of hydro-mechanical loading. In: *Mechanical Behaviour of Salt VIII*. CRC Press, pp. 217–227–.
- Minkley, W., Menzel, W., Konietzky, H., te Kamp, L., 2001. A visco-elasto-plastic softening model and its application for solving static and dynamic stability problems in potash mining. In: et al., D. B. (Ed.), *FLAC and*

- Numerical Modeling in Geomechanics – 2001 (Proceedings of the 2nd International FLAC Conference, Lyon, France). pp. 27–27.
- Minkley, W., Mühlbauer, J., 2007. Constitutive models to describe the mechanical behavior of salt rocks and the imbedded weakness planes. In: Wallner, M., Lux, K., Minkley, W., Hardy, H. (Eds.), *The Mechanical Behaviour of Salt – Understanding of THMC Processes in Salt: 6th Conference (SaltMech6)*, Hannover, Germany. pp. 119–127.
- Minkley, W., Mühlbauer, J., Lüdeling, C., 2015. Dimensioning Principles in Potash and Salt Mining to Achieve Stability and Integrity. In: *49th US Rock Mechanics/Geomechanics Symposium*. American Rock Mechanics Association.
- Nagel, T., Görke, U.-J., Moerman, K. M., Kolditz, O., 2016. On advantages of the Kelvin mapping in finite element implementations of deformation processes. *Environmental Earth Sciences* 75 (11), 1–11.
- Nagel, T., Minkley, W., Böttcher, N., Naumov, D., Görke, U.-J., Kolditz, O., 2017. Implicit numerical integration and consistent linearization of inelastic constitutive models of rock salt. *Computers & Structures* 182, 87–103.
- Niazi, M., Wisselink, H., Meinders, T., 2013. Viscoplastic regularization of local damage models: revisited. *Computational mechanics*, 1–14.
- Ozarslan, A., 2012. Large-scale hydrogen energy storage in salt caverns. *International Journal of Hydrogen Energy* 37 (19), 14265 – 14277, {HYFUSENSpecial} Issue for the 4th National - 3rd Latin American Conference on Hydrogen and Sustainable Energy Sources (HYFUSEN), 6-9 June 2011, Mar Del Plata, Argentina.
- Peng, D.-Y., Robinson, D. B., 1976. A New Two-Constant Equation of State. *Industrial & Engineering Chemistry Fundamentals* 15 (1), 59–64.
- PowerSouth Energy Cooperative, 2012. McIntosh Power Plant. Brochure.
- Pudewills, A., 2005. Numerical modelling of the long-term evolution of EDZ: Development of material models, implementation in finite-element codes, and validation. *Wissenschaftliche Berichte FZKA 7185*.
- Pudewills, A., Droste, J., 2003. Numerical modeling of the thermomechanical behavior of a large-scale underground experiment. *Computers & Structures* 81 (8), 911–918.
- Pudewills, A., Müller-Hoeppe, N., Papp, R., 1995. Thermal and thermomechanical analyses for disposal in drifts of a repository in rock salt. *Nuclear Technology* 112 (1), 79–88.
- Sachse, A., Nixdorf, E., Jang, E., Rink, K., Fischer, T., Xi, B., Beyer, C., Bauer, S., Walther, M., Sun, Y., Song, Y., 2017. *OGS Tutorial: Computational Hydrology II: Groundwater Quality Modeling*. Springer-Verlag GmbH.
- Sachse, A., Rink, K., He, W., Kolditz, O., 2015. *OpenGeoSys Tutorial: Computational Hydrology I: Groundwater Flow Modeling*. Springer-Verlag GmbH.

- Safaei, H., Keith, D. W., Hugo, R. J., 2013. Compressed air energy storage (CAES) with compressors distributed at heat loads to enable waste heat utilization. *Applied Energy* 103 (0), 165–179.
- Seifert, T., Schmidt, I., 2008. Line-search methods in general return mapping algorithms with application to porous plasticity. *International journal for numerical methods in engineering* 73 (10), 1468–1495.
- Shao, H., Hein, P., Sachse, A., Kolditz, O., 2016. *Geoenergy Modeling II*. Springer-Verlag GmbH.
- Sicsic, P., Bérest, P., 2014. Thermal cracking following a blowout in a gas-storage cavern. *International Journal of Rock Mechanics and Mining Sciences* 71, 320 – 329.
- Simo, J. C., Hughes, T. J. R., 1998. Objective Integration Algorithms for Rate Formulations of Elastoplasticity. In: *Computational Inelasticity*. Vol. 7 of *Interdisciplinary Applied Mathematics*. Springer New York, pp. 276–299.
- Sriapai, T., Walsri, C., Fuenkajorn, K., 2012. Effect of temperature on compressive and tensile strengths of salt. *ScienceAsia* 38 (2), 166–174.
- Taylor, J., Alderson, J., Kalyanam, K., Lyle, A., Phillips, L., 1986. Technical and economic assessment of methods for the storage of large quantities of hydrogen. *International Journal of Hydrogen Energy* 11 (1), 5 – 22.
- Wang, G., Guo, K., Christianson, M., Konietzky, H., 2011. Deformation characteristics of rock salt with mudstone interbeds surrounding gas and oil storage cavern. *International Journal of Rock Mechanics and Mining Sciences* 48 (6), 871–877.
- Wang, W., Sluys, L., De Borst, R., 1997. Viscoplasticity for instabilities due to strain softening and strain-rate softening. *International Journal for Numerical Methods in Engineering* 40 (20), 3839–3864.(1997).
- Watanabe, N., Blöcher, G., Cacace, M., Held, S., Kohl, T., 2017. *Geoenergy Modeling III*. Springer-Verlag GmbH.
- Xia, C., Zhou, Y., Zhou, S., Zhang, P., Wang, F., 2015. A simplified and unified analytical solution for temperature and pressure variations in compressed air energy storage caverns. *Renewable Energy* 74, 718–726.
- Xing, W., Zhao, J., Hou, Z., Were, P., Li, M., Wang, G., 2015. Horizontal natural gas caverns in thin-bedded rock salt formations. *Environmental Earth Sciences* 73 (11), 6973–6985.
- Zienkiewicz, O. C., Taylor, R. L., Zhu, J. Z., 2005-2006. *The finite element method set*, 6th Edition. Elsevier Butterworth-Heinemann, Oxford.